A time-domain second-order FEM model for the wave diffraction-radiation problem. Validation with a semisubmersible platform.

Borja Servan-Camas[a,*], Jose E. Gutierrez-Romero[b], Julio Garcia-Espinosa[a,c]

(a) Centre Internacional de Metodes Numerics en Enginyeria (CIMNE),http://www.cimne.upc.edu/
Edifici C1, Campus Norte, UPC, Gran Capitán s/n, 08034 Barcelona, Spain
(b) Depart. Naval Technology, Universidad Politécnica de Cartagena (UPCT), http://www.upct.es/,
Paseo Alfonso XIII 48, 30203 Cartagena, Spain
(c) Universidad Politécnica de Cataluña (UPC), C. Gran Capitan s/n, Campus Nord, 08034 Barcelona, Spain.
(*) Corresponding autor.

Abstract

A finite element method for the solution of the up-to-second-order wave diffraction-radiation problem in the time-domain is proposed. The solver has been verified against available analytical solutions, and validated against experimental data available for the HiPRWind semisubmersible platform (designed for floating wind turbines). To perform the validation, the wave diffraction-radiation solver is coupled to a body dynamics and mooring solvers in the time-domain. The HiPRWind movements and mooring forces have been compared for a large number of test cases, including decay tests, monochromatic waves, bichromatic and irregular waves. Good agreement has been found for both, body movements and mooring forces.

1. Introduction

There is a growing focus of the industry on Floating Offshore Wind Turbines (FOWT) due to their ability to access the enormous wind resources available over deep water. Despite the existence of real scale prototypes already operating, such as the Hywind in Norway [1] or the Windfloat in Portugal [2], the industry still faces design and operation challenges which require the development of new modeling tools to be overcome. In this work, we propose a model to analyze the up-to-second-order response of floating structures, which is validated with experimental tests conducted for the HiPRWind semisubmersible FOWT model. A review on floating offshore wind technology can be found in [3,4,5].

The hydrodynamics of the semisubmersible concept for FOWTs has received some attention in the recent literature. For instance, [6] and [7] focused on slow-drift and mean-drift forces of semisubmersible platforms, a comparison of a semisubmersible against a SPAR concept can be found in [8,9,10], and

simulations in the Time-Domain (TD) considering different models for the hydrodynamic loads were carried out in [11].

One of the main concerns regarding semisubmersible platforms is the slow-drift forces. These forces are usually in the range of the surge natural period of the semisubmersible platform with catenary mooring lines, leading to large displacements when excited near the resonance frequency. And although the wave frequencies are usually larger than the natural frequencies, second-order effects contain low frequencies components that might excite slow-drift in the system platform-mooring. This might lead to large excursions.

Second-order forces might increase the surge response of semisubmersible platforms, even becoming larger that the first-order response. And although Newman's approximation -which only depends on the first-order solution- could be used for estimating the slow-drift forces, it might not be precise enough as shown in [7]. Hence, second-order effect must be taken into account to accurately compute slow-drift motions, and design the mooring system accordingly.

The impact of the slow-drift forces on the design of the mooring systems and the difficulties to estimate the corresponding forces is yet a problem that requires substantial research. Let's remind that the mooring system must restrain the floater excursions within predefined limits.

The design of the mooring system is based on loads induced by the excursions. These can be predicted on an extensive set of TD simulations comprising different environmental conditions (combinations of waves, current, and wind conditions). This set aims at representing the metocean statistics of the specific location. In these simulations, wave loads are usually taken into account using Frequency-Domain (FD) results as inputs (added masses, potential damping, excitation forces, or impulse response functions). And these inputs are obtained from a radiation-diffraction code.

Quadratic transfer functions (QTFs) obtained by frequency domain solvers are usually used as inputs for second-order time-domain simulations. But these QTFs depend on linear first-order response amplitude operators (RAOs). Hence, in case where the mooring lines are not linear (like the catenary lines used for semisubmersible platforms), these have to be linearized so that RAOs can be obtained. Therefore, QTFs obtained in the frequency-domain do not contain information about the nonlinear behavior of the mooring. A direct diffraction-radiation TD solver, like the one to be presented in this work, accounts for this sort of nonlinearities in a natural way.

Apart from the importance of second-order effects on the dynamic response of floating structures, recent works have emphasized the importance of the second-order effects on the surge response of FOWT. Coulling et al. [12] concluded that particular attention must be paid to motion and load responses of the platforms associated with the second-order difference-frequency forces of environmental wave loads, since the exclusion of the second-order dynamic analysis leads to a reduction of the platform mean excursions. Other works [13,14] have recently assessed the effects of second-order hydrodynamics on semisubmersible FOWT which usually are neglected in the dynamic behaviour of FOWT. These forces lead to large oscillations that strain the mooring system or vibrations that cause fatigue damage to the moored structure. And Luptom and Langley state in [6] that slow-drift forces might be less important for FOWT than for larger and better known floating structures such as those used in the oil industry. Anyhow, accurate estimation of these forces is mandatory to assess its impact.

More recently, Lopez-Pavon et al. [7] and Simos et al. [15] focused on the estimation and verification of the second-order wave induced forces on the HiPRWind semisubmersible platform. This work concludes with the following statements:

1. Accurate calculation of the second-order forces may be difficult to guarantee and it is not unusual that different numerical codes (based on different approximations for these forces) may render somewhat divergent results.
2. The experimental verification of the slow-drift effects is quite difficult. Accurate measurement of the low-frequency forces is hard to obtain and indirect verifications based on the resonant motions of the floating body depend on other factors such as the viscous damping of the small-scale model, the geometrical characteristics of the mooring system, etc.

In this work, a Finite Element Method (FEM) that solves the up-to-second-order wave diffraction-radiation problem in the time-domain is proposed. In this TD model, non-linear forces such as those arising from the mooring lines can be introduced straightforward into the dynamics of the floater with no need of linearization. First, the mathematical and numerical models for the wave diffraction-radiation problem are presented. Then a verification of the model is carried out comparing to second-order analytical solutions available. Afterwards, a model of the HiPRWind platform is calibrated using decay tests and then analyzed in monochromatic, bichromatic and irregular waves to validate the proposed numerical approach. Finally some conclusions are made regarding the model presented and the results obtained.

2. *Up-to-second-order diffraction-radiation governing equations*

The potential flow governing equations for the up-to-second-order wave problem are obtained by applying Taylor expansion on the boundary surfaces of a time-independent domain. This approach allows to approximate the free surface on $z = \xi$ and the mean wetted surface S_B of a floating body at time t. Then, a perturbed solution based on the Stokes expansion procedure is applied to the velocity potential, the free surface elevation, and the floater motion. Retaining terms up to second order, the resulting equations are:

$$\Delta\phi^{1+2} = 0 \qquad in\ \Omega, \tag{1}$$

$$\frac{\partial\eta^{1+2}}{\partial t} - \frac{\partial\phi^{1+2}}{\partial z} = -S^1 \qquad in\ z = 0, \tag{2}$$

$$\frac{\partial\phi^{1+2}}{\partial t} + \frac{P_{fs}}{\rho} + g\eta^{1+2} = -R^1 \qquad in\ z = 0, \tag{3}$$

$$v_\phi^{1+2} \cdot n_p^0 + v_\phi^1 \cdot n_p^1 = -\left(v_p^1 + v_\psi^1\right) \cdot n_p^1 - \left(v_p^{1+2} + v_\psi^{1+2} + r_p^1 \cdot \left(\nabla v_\phi^1 + \nabla v_\psi^1\right)\right) \cdot n_p^0 \qquad on\ P \in S_B^0, \tag{4}$$

$$R^1 = \eta^1 \frac{\partial}{\partial z}\left(\frac{\partial\phi^1}{\partial t}\right) + \zeta^1 \frac{\partial}{\partial z}\left(\frac{\partial\phi^1}{\partial t}\right) + \eta^1 \frac{\partial}{\partial z}\left(\frac{\partial\psi^1}{\partial t}\right) + \frac{1}{2}\nabla\phi^1 \cdot \nabla\phi^1 + \nabla\psi^1 \cdot \nabla\phi^1, \tag{5}$$

$$S^1 = \frac{\partial\phi^1}{\partial \mathrm{x}}\frac{\partial\eta^1}{\partial x} + \frac{\partial\phi^1}{\partial \mathrm{y}}\frac{\partial\eta^1}{\partial y} + \frac{\partial\phi^1}{\partial \mathrm{x}}\frac{\partial\zeta^1}{\partial x} + \frac{\partial\phi^1}{\partial \mathrm{y}}\frac{\partial\zeta^1}{\partial y} + \frac{\partial\psi^1}{\partial \mathrm{x}}\frac{\partial\eta^1}{\partial x} + \frac{\partial\psi^1}{\partial \mathrm{y}}\frac{\partial\eta^1}{\partial y}, \tag{6}$$

where superscripts 1 and $1+2$ denote the components at the first-order and up-to-second-order solution (first order plus second order), respectively, ψ^{1+2} is the up-to-second-order incident wave velocity potential, ζ^{1+2} is the up-to-second-order incident free surface elevation, ϕ^{1+2} and η^{1+2} are the up-to-second-order diffraction-radiation wave velocity potential and free surface elevation, respectively, P_{fs} is the free surface pressure, S_B^0 is the mean wetted body surface, v_p^i is the local velocity induced at point P by the body i-th order movements, v_ϕ^i is the i-th order fluid velocity induced by the diffracted-radiated waves, v_ψ^i is the i-th order fluid velocity induced by the incident waves, n_p^i is the normal vector to the body surface S_B^i at point P. The fluid pressure at a point P on the body surface is given by:

$$P_p^{1+2} = P_{ph}^0 + P_{ph}^{1+2} + P_{p\psi}^{1+2} + P_{p\phi}^{1+2}, \tag{7}$$

where P_{ph}^i, $P_{p\psi}^i$, and $P_{p\phi}^i$ stand for the i-th order hydrostatic, incident wave induced, and diffracted-radiated waves induced pressures, respectively. Each pressure component is further decomposed as:

$$\begin{aligned} P_{ph}^0 &= -\rho g z_p, \\ P_{ph}^{1+2} &= -\rho g r_{pz}^{1+2}, \\ P_{p\phi}^{1+2} &= -\rho \frac{\partial \phi^{1+2}}{\partial t} - \rho \frac{1}{2} \nabla \phi^1 \cdot \nabla \phi^1 - \rho \nabla \psi^1 \cdot \nabla \phi^1 - \rho r_p^1 \cdot \nabla \left(\frac{\partial \phi^1}{\partial t} \right), \end{aligned} \tag{8}$$

where r_p^i represents the displacement of point P induced by the i[th] order body movement (see Figure 1). Further details on obtaining the governing equations can be found in Servan-Camas and Garcia-Espinosa [16], and Servan-Camas [17].

The body dynamics of the floating body are governed by the equation of motion:

$$\overline{\overline{\mathbf{M}}}\, \mathbf{X}_{tt} + \overline{\overline{\mathbf{K}}}\, \mathbf{X} = \mathbf{F} \tag{9}$$

where $\overline{\overline{\mathbf{M}}}$ is the mass matrix of the body, $\overline{\overline{\mathbf{K}}}$ is the hydrostatic restoring matrix (approximates the integral of the hydrostatic pressure), $\mathbf{F}$ is the vector of the hydrodynamic forces induced by dynamic pressures plus any other external forces, and $\mathbf{X}$ represent the movements of the six degrees of freedom of the body.

Loads acting on the body are obtained by direct pressure integration on the body surface underneath the mean water level, except for the hydrostatic forces, which are obtained via the corresponding hydrostatic restoring matrices. Also, the second-order loads ($\boldsymbol{F}_{wl}^2$ and $\boldsymbol{M}_{wl}^2$) due to the change of the wetted surface induced by the first order solution are accounted for:

$$\begin{aligned} \boldsymbol{F}_{wl}^2 &= -\frac{1}{2}\rho g \int_{\Gamma_{wl}^0} \left(\xi^1 - r_{pz}^1\right)^2 \frac{\boldsymbol{n}_p^0}{\sqrt{1 - {n_{pz}^0}^2}} dl, \\ \boldsymbol{M}_{wl}^2 &= -\frac{1}{2}\rho g \int_{\Gamma_{wl}^0} \left(\xi^1 - r_{pz}^1\right)^2 \overrightarrow{\boldsymbol{G}^0\boldsymbol{P}^0} \times \frac{\boldsymbol{n}_p^0}{\sqrt{1 - {n_{pz}^0}^2}} dl. \end{aligned} \tag{10}$$

where $\overrightarrow{\boldsymbol{G}^0\boldsymbol{P}^0}$ is the vector from the center of gravity of the floater G to any point P on the wet surface.

3. Numerical model

3.1 Finite element formulation

This section presents the formulation based on the Finite Element Method (FEM) to solve the system of equations governing the wave diffraction-radiation problem. This formulation has been developed to be used in conjunction with unstructured meshes in order to enhance geometry flexibility and speed up the initial modelling time.

Let Q_h^* be the finite element space to interpolate functions, constructed in the usual manner. From this space, it can be constructed the subspace $Q_{h,\phi}^*$, that incorporates the Dirichlet conditions for the potential ϕ. The space of test functions, denoted by Q_h, is constructed as $Q_{h,\phi}$, but with functions vanishing on the Dirichlet boundary. The weak form of the problem can be written as follows:

Find $[\phi_h] \in Q_{h,\phi}^*$, by solving the discrete variational problem:

$$\int_{\Omega} \nabla v_h \cdot \nabla \phi_h \, \mathrm{d}\Omega = \int_{\Gamma^{\mathrm{B}}} v_h \cdot \hat{\phi}_n^B \, \mathrm{d}\Gamma + \int_{\Gamma^{\mathrm{R}}} v_h \cdot \hat{\phi}_n^R \, \mathrm{d}\Gamma + \int_{\Gamma^{Z_0}} v_h \cdot \hat{\phi}_n^{Z_0} \mathrm{d}\Gamma + \int_{\Gamma^{Z-\mathrm{H}}} v_h \cdot \hat{\phi}_n^{Z-H} \mathrm{d}\Gamma \quad \forall v_h \in Q_h, \tag{11}$$

where $\hat{\phi}_n^B$, $\hat{\phi}_n^R$, $\hat{\phi}_n^{Z_0}$ and $\hat{\phi}_n^{Z-H}$ are the potential normal gradients corresponding to the Neumann boundary conditions on bodies, radiation boundary, free surface and bottom surface of the domain, respectively. At this point, it is useful to introduce the associated matrix form of Eq.(11):

$$\bar{\bar{\mathbf{L}}}\boldsymbol{\phi} = \mathbf{b}^B + \mathbf{b}^R + \mathbf{b}^{Z_0} + \mathbf{b}^{Z-H}, \tag{12}$$

where $\bar{\bar{\mathbf{L}}}$ is the standard Laplacian matrix, and $\mathbf{b}^B$, $\mathbf{b}^R$, and $\mathbf{b}^{Z_0}$, and $\mathbf{b}^{Z-H}$ are the vectors resulting of integrating the corresponding boundary condition terms. Regarding the seabed boundary for the refracted and radiated potential, it is imposed naturally in the formulation by taking $\mathbf{b}^{Z-H} = 0$.

3.2 Free surface boundary conditions

Combining the kinematic (Eq. (2)) and dynamic (Eq. (3)) free surface boundary conditions, the free surface condition up to second order reads:

$$\frac{\partial^2\phi}{\partial t^2} + g\frac{\partial\phi}{\partial z} + \frac{\partial}{\partial t}\left(\frac{P_{fs}}{\rho}\right) + \{Q^1\} = 0. \tag{13}$$

where superscripts 1+2 have been omitted (and will be from this point on), and Q^1 are the source terms from the first-order solution. This condition is implemented as a Neumann boundary condition that fulfils the flux boundary integral:

$$\mathbf{b}^{Z_0} = \bar{\bar{\mathbf{M}}}_{\Gamma Z_0}\hat{\phi}_n^{Z_0}, \tag{14}$$

where $\bar{\bar{\mathbf{M}}}_{\Gamma Z_0}$ is the corresponding boundary mass. The terms R^1 and S^1 are given by Eqs. (5) and (6) respectively, then:

$$Q^1 = \partial_t R^1 - S^1, \tag{15}$$

Eq. (13) is discretized in time using the following numerical scheme:

$$\frac{\phi^{n+1} - 2\phi^n + \phi^{n-1}}{\Delta t^2} = -g\phi_z^n - \frac{1}{12}g(\phi_z^{n+1} + 10\phi_z^n + \phi_z^{n-1}) - \frac{P_{fs}^{n+1} - P_{fs}^{n-1}}{\rho 2\Delta t} - \left\{\frac{1}{12}((Q^1)^{n+1} + 10(Q^1)^n + (Q^1)^{n-1})\right\}, \tag{16}$$

where for the specific case where $P_{fs} = 0$, the above scheme becomes a fourth order compact Padé scheme. Once the velocity potential is solved at the new time step, the free surface elevation is computed using the following fourth-order in time numerical scheme:

$$\eta^{n+1} = -\frac{1}{g\Delta t}\left(\frac{25}{12}\phi^{n+1} - 4\phi^n + 3\phi^{n-1} - \frac{4}{3}\phi^{n-2} + \frac{1}{4}\phi^{n-3}\right) - \frac{P_{fs}^{n+1}}{\rho g}\{-(S^1)^{n+1}\}. \tag{17}$$

3.3 Radiation condition and wave absorption

Waves represented by ϕ are born at the bodies and propagate in all directions away from them. These waves have to either be dissipated or to be let go out of the domain so they will not bounce back to interact with the bodies. Then a Sommerfeld radiation condition at the edge of the computational domain is introduced:

$$\partial_t\phi + c\nabla\phi \cdot n_R = 0 \qquad in\ \Gamma_R, \tag{18}$$

where Γ_R is the surface limiting the domain in the horizontal directions, n_R is the normal vector of Γ_R pointing outwards the domain, and c is a prescribed wave phase velocity. This radiation condition will let waves moving at velocity c to escape out of the domain. The numerical scheme used to implement the radiation condition is

$$(\phi_{\boldsymbol{n}}^{R})^{n+1} = -\frac{\phi^{n-1} - \phi^{n}}{c\Delta t} \qquad in\ \Gamma_R. \tag{19}$$

The prescribed phase velocity c will be set for radiating those waves with the smallest frequency (largest wavelengths) considered in each specific case under study. Typical value of c is the phase velocity of the longer incident wave. However, waves with higher frequencies (smaller phase velocities) will not leave the domain through Γ_{R}, so that they will be reflected. Hence, wave absorption is introduced into the dynamic free surface boundary condition by varying the pressure such that:

$$P_{fs}(\boldsymbol{x}, t) = \kappa(\boldsymbol{x})\rho\frac{\partial\phi}{\partial z}. \tag{20}$$

Eq. (20) increases pressure when the free surface is moving upwards, while decreases the pressure when the free surface is moving downwards. Then energy is transferred from the waves to the atmosphere and waves are damped. However, the coefficient $\kappa(\boldsymbol{x})$ will be set to zero in the analysis area (near the bodies), so that damping will have no effect on the solution of the wave-body interaction problem. Further details can be found in Servan-Camas and Garcia-Espinosa[16] and Servan-Camas [17].

4. Mooring models

Two different computational models have been implemented in the seakeeping solver to simulate the mooring lines. The first one is an elastic catenary solver, and the second one is a non-linear FEM dynamic cable solver. In the following sections, a brief description of the mathematical model is given. Details on the numerical implementation of the mooring solver, the body dynamics solver, and their coupling can be found in [17,18,19,20].

4.1 Elastic Catenary model

The elastic catenary formulation is based on the model proposed in [21]. Each mooring line is analysed in a local coordinate system located at the anchor. The local z-axis is oriented vertical and the local x-axis is oriented horizontally from the anchor to the instantaneous position of the fairlead. When a portion of

the mooring line rests on the seabed, the equations for the horizontal and vertical distances between the anchor and a given point on the line, $x(s)$ and $z(s)$, can be written as,

$$x(s) = \begin{cases} s & \text{for } 0 \le s \le L_B - \frac{H_F}{C_B\omega}, \\ s + \frac{C_B\omega}{2EA}\left[s^2 - 2\left(L_B - \frac{H_F}{C_B\omega}\right)s + \left(L_B - \frac{H_F}{C_B\omega}\right)\max\left(\left(L_B - \frac{H_F}{C_B\omega}\right), 0\right)\right] & \text{for } L_B - \frac{H_F}{C_B\omega} \le s \le L_B, \\ L_B + \frac{H_F}{\omega}\ln\left[\frac{\omega(s-L_B)}{H_F} + \sqrt{1 + \left(\frac{\omega(s-L_B)}{H_F}\right)^2}\right] + \frac{H_F L}{EA} & \text{for } L_B \le s \le L, \\ \quad + \frac{C_B\omega}{2EA}\left[-L_B^2 + \left(L_B - \frac{H_F}{C_B\omega}\right)\max\left(\left(L_B - \frac{H_F}{C_B\omega}\right), 0\right)\right] & \end{cases} \tag{21}$$

$$z(s) = \begin{cases} 0 & \text{for } 0 \le s \le L_B - \frac{H_F}{C_B\omega}, \\ \frac{H_F}{\omega}\sqrt{1 + \left(\frac{\omega(s-L_B)}{H_F}\right)^2} + \frac{\omega(s-L_B)^2}{2EA} & \text{for } L_B \le s \le L, \end{cases} \tag{22}$$

being s the catenary arc length, H_F the horizontal component of the effective tension, C_B static friction coefficient, ω catenary weight per unit length in water, E the Young modulus, A the cross section area and L_B portion of the length of cable resting at the seabed.

The equation for the effective tension in the line at any point of the line $T(s)$ is written as follows:

$$T(s) = \begin{cases} \max(H_F + C_B\omega(s - L_B), 0) \\ \sqrt{H_F^2 + (\omega(s-L_B)^2)} \quad \text{for } L_B \le s \le L \end{cases}. \tag{23}$$

The above formulation leads to a computation of the total load on the system from the contribution of all mooring lines. The restoring load is found by first transforming each fairlead tension from its local coordinate system to the global frame, and then summing up the tensions from all lines.

4.2 Dynamic cable model

The dynamic equations for a mooring cable with length L with negligible bending and torsional stiffness can be formulated as [18]:

$$(\rho_w C_m A_0 + \rho_0)\frac{\partial^2 r_l}{\partial t^2} = \frac{\partial}{\partial l}\left(EA_0 + \frac{e}{e+1}\frac{\partial r_l}{\partial l}\right) + \mathrm{f}(t)(1+e), \tag{24}$$

where ρ_w is the water density, C_m is the added mass coefficient, ρ_0 is the mass per unit length of the unstretched cable, r_l is the position vector, E is the Young's modulus, A_0 is the cross-sectional area of the

cable, e is the strain, $\mathrm{f}(t)$ are the external loads applied on the cable including the self-weight, hydrostatic loads, drag forces and seabed interaction, and l is the length along the unstretched cable.

The boundary conditions of the mooring cable are given by

$$\frac{\partial^2 r_l}{\partial t^2} = 0, \text{at } l = 0, (anchor\ point), \tag{25}$$

$$\frac{\partial^2 r_l}{\partial t^2} = \ddot{r}_b, \text{at } l = L, (fairlead\ point), \tag{26}$$

where $\ddot{r}_b$ is the second derivative of the position vector at the fairlead connection point.

The above non-linear equation is solved using the standard Finite Element Method. Details about the mathematical and numerical dynamic model are provided in Gutierrez-Romero et al. [18].

5. Numerical model verification

5.1 Verification case 1: mean drift forces on a hemisphere

5.1.1 Problem description

This case consists of estimating the mean drift forces on a hemisphere. In this work, mean drift forces are obtained by time averaging the time series of the corresponding second-order force. The analytical solution for the fix hemisphere was obtained by Fernandes and Levy [22], and for the freely floating hemisphere was obtained by Kudou [23] and reported by Pinkster [24]. In this section, the numerical results are compared against the analytical solution. The hemisphere particulars are given in Table 1. Both fixed and free floating cases were analyzed. Figure 2 (left) shows the mesh used for the calculations. It can be observed that mesh refinement is required in the area of the waterline in order to obtain accurate results of mean drift forces. Figure 2 (right) shows a snapshot of the wave elevation around the hemisphere in one of the cases run. Finally, Figure 3 (up) compares the analytical results against the numerical results in the case of the fixed hemisphere, while Figure 3 (down) compares the results in the free floating case. A good agreement is observed for the whole range of waves analyzed.

Table 1: hemisphere particulars.

Depth	Infinite
Mass	Displacement

Radius	1m
CG	(0,0,0)
Number of tetrahedrons	274283
Number of triangles	22082

5.2 Verification case 2: diffraction of second-order monochromatic waves by semisubmerged horizontal rectangular cylinder

5.2.1 Problem description

This test case deals with the solution to the diffraction problem for second-order monochromatic surface waves by a semisubmerged horizontal cylinder of rectangular cross section. The boundary-value problem is solved and the results are compared against the analytical solution obtained by the method of matched Eigen function expansions presented in [25]. Horizontal and vertical forces and the moment about the heel of the prismatic cylinder are analyzed for different monochromatic waves. A sketch of the problem under analysis is shown in Figure 4. Relevant geometry parameters are: depth (h = 1 m), half beam (b = 1 m), and draught (d = 0.2 m).

The situation considered for analysis is the diffraction of waves by a fixed horizontal cylinder of rectangular cross section. The analysis is undertaken with the following assumptions: the fluid is inviscid and incompressible, the sea bottom and the cylinder are impervious, and the excitation is provided by normally incident plane waves of small amplitude and frequency. Several cases are run for different wave periods (T = 0.897, 1.003, 1.070, 1.160, 1.445, 2.299, 4.170, and 6.370 seconds), and the simulation time is about 30 seconds, with an initialization time of 10 seconds. All degrees of freedom are restrained so that the body is completely fixed. Hence, only wave diffraction occurs but not radiation.

5.2.2 Mesh generation

Mesh properties for the present analysis are summarized in Table 2. Figure 5 shows an isometric view of the mesh used for the present analysis at the region close to the surface of the body.

Table 2: Verification case 2: mesh particulars.

Minimum element size	0.01
Maximum element size	0.1
Number of elements	121687
Number of nodes	22940

5.2.3 Verification of results

Figure 6 shows the amplitude of the second-order horizontal force(F_x), vertical force (F_z) forces, and moment about y axis, M_y, for both the analytical results reported in [25] and the numerical results obtained in this work. The second-order components of the forces and moments (double frequency component) are normalized with $\rho g h A^2$, where ρ is the density of the fluid, g the gravity, A^2 the square of the wave amplitude, and h the water depth. Results are plotted against the dimensionless wave number (kh). As it can be observed, a good agreement is obtained for the analyzed range of wave numbers.

5.3 Verification case 3: diffraction of second-order bichromatic waves by bottom mounted circular cylinder

5.3.1 Problem description

This test case deals with the diffraction of a bottom mounted vertical cylinder under monochromatic waves with water depth $h = 4$ m, radius of the cylinder $R = 1$ m (see [26]).

5.3.2 Convergence analysis

A convergence analysis has been carried out to assess the convergence of the present numerical approach to the mathematical model. Table 3 provides the unstructured mesh particulars for each case tested. Table 4 provides the dimensionless force along the wave direction. In particular, the dimensionless force for the sum-frequency is analyzed. The wave frequencies chosen for this analysis are $\omega_1 R/g = 1.4$ and $\omega_2 R/g = 2.0$. Time step is calculated such that $g\Delta t^2/h = 0.34$, being h the characteristic element size at the floating line. The results in table 3 shows that the convergence rate is approximately second order, although care must be taken since convergence tests on unstructured meshes contains uncertainties due to the irregularity on the shape of the elements.

Table 3: Convergence test: mesh particulars.

	Characteristic element size [m]				Number of elements	Number of nodes
	Floating line h	Body and free surface	Volume	Δt [s]		
Mesh 1	0.1	0.2	0.4	0.0587	727221	125926
Mesh 2	0.071	0.1414	0.2828	0.0494	983719	169908
Mesh 3	0.05	0.1	0.2	0.0415	1683943	289527
Mesh 4	0.035	0.0707	0.1414	0.0349	3475047	594852
Mesh 5	0.025	0.05	0.1	0.0294	8203778	1399855

Table 4: Convergence analysis: values of the sum-frequency dimensionless force for $\omega_1 R/g = 1.4$ and $\omega_2 R/g = 2.0$.

	Mesh 1	Mesh 2	Mesh 3	Mesh 4	Mesh 5
h	0.1	0.071	0.05	0.035	0.025
F_x^*	2.498	2.348	2.229	2.159	2.141
Relative Error	-	0.150	0.119	0.070	0.018

5.3.3 Verification of results

Table 5 shows a comparison for the non-dimensional amplitude for the sum-frequency and difference-frequency forces along the wave direction. Mesh 4 has been used to carry out all cases presented. Comparing to the results obtained by other authors, it can be observed that the results obtained in this work are within the range of the ones reported by the others.

Table 5: Comparison of non-dimensional amplitude of the sum-frequency and difference-frequency forces along the wave direction.

	$\frac{\omega_1 R}{g} = 1.0\ \frac{\omega_2 R}{g} = 1.6$		$\frac{\omega_1 R}{g} = 1.2\ \frac{\omega_2 R}{g} = 1.8$		$\frac{\omega_1 R}{g} = 1.4\ \frac{\omega_2 R}{g} = 2.0$	
	sum-freq	diff-freq	sum-freq	diff-freq	sum-freq	diff-freq
Shao and Faltinsen [27]	1.868	0.861	2.190	0.788	2.088	0.759
Kim and Yue [28]	1.853	0.856	2.182	0.788	2.094	0.765
Eatock Taylor and Huang [26]	1.883	0.849	2.294	0.769	2.114	0.777
Moubayed and Williams [29]	1.783	0.840	2.091	0.761	1.998	0.734
Present work	1.815	0.852	2.248	0.765	2.159	0.740

6. Validation against the HiPRWind model

6.1 Case description

The floating platform geometry considered in this paper has been provided by the HiPRWind FP7 project (EU 7th RTD FP under grant agreement no. 256812) [30] and is composed by three buoyant columns connected by bracings. Model tests were carried out at Ecole Centrale Nantes' facilities. A model built in stainless steel with scale $\lambda = 1/19.8$ was used in the tests (see Figure 7). The experiments were devised by Simos et al. [15] in order to use the measured motions to validate an alternative method to

estimate, in the frequency domain, the second order response of the floater. Results related to mooring loads are however presented herein for the first time.

Figure 8 shows an overview of the HiPRWind CAD model generated. Table 6 provides the platform particulars in full scale, as well as the water depth considered for this study.

Table 6: HiPRWind platform main particulars (full scale).

Depth	100 m
Operation design draft	15.5 m
Distance between column centers	35 m
Column diameter	7 m
Heave plates diameter	20 m
Displacement	2332 T
XG	0 m
YG	0 m
ZG	-4.46 m
Radius of gyration (pitch)	22.38 m

Figure 9 shows a view of the mesh used for this case study. This mesh consists of tetrahedral 643603 elements and 119350 nodes. The cylindrical domain has a radius of 500 meters, a height of 100 m water depth, and the absorption area starts at 50 meters from the center of the platform.

6.2 Model calibration

In order to predict seakeeping in real conditions with a potential flow solver, viscous effects are to be incorporated via external forces. These external forces are simplified formulas accounting for the overall viscous effects acting on the platform. In this work, the viscous effects have been included in the computational solver by means of linear and quadratic models. This model has been calibrated using the experimental information of the extinction tests for surge, heave and pitch motions.

Figure 10 shows the layout of the experimental set-up for these tests. Three elastic lines were used to keep the position of the model during the extinction experiments. These lines have a small linear weight distribution so the catenary effect is negligible. The location of the end points for each line is given in Table 7. A pretension of 550 kN were applied to each line.

Table 7: Mooring lines end points and stiffness coefficients.

	(x_i, y_i, z_i)	(x_f, y_f, z_f)	K(KN/m)
Line 1	$(-323.75, 0, 10)$	$(-23.73, 0, 10)$	20.8
Line 2	(207.7,250.4,10)	$(11.87, 20.55, 10)$	20.8
Line 3	$(207.7, -250.4, 10)$	$(11.87, -20.55, 10)$	20.8

The linear stiffness matrix corresponding to the mooring system is:

$$K_{mooring} = \begin{bmatrix} 3.65\times10^4 & 0 & 0 & 0 & 3.65\times10^4 & 0 \\ 0 & 2.35\times10^4 & 0 & -2.35\times10^5 & 0 & 1.26\times10^5 \\ 0 & 0 & 0 & 0 & 0 & 0 \\ 0 & -2.35\times10^5 & 0 & 1.96\times10^7 & 0 & -1.26\times10^6 \\ 3.65\times10^5 & 0 & 0 & 0 & 2.51\times10^7 & 0 \\ 0 & 1.26\times10^5 & 0 & 3.09\times10^5 & 0 & 3.94\times10^7 \end{bmatrix}.$$

The viscous damping forces have been divided into two groups. The first group corresponds to the bracings of the structure. The corresponding forces are applied in the center of gravity of the platform. The second group corresponds to the heave plates and columns, and calibration forces are applied in the center of the heave plates assuming a dominant effect of these over the cylinders. Table 8 provides a summary of the coefficients of the damping terms obtained in the calibration phase. A similar calibration process for the BEM frequency domain solver WADAM [31] has also been performed by an independent engineer, resulting in quite similar calibration values.

Table 8: Model calibration: added mass, linear damping and quadratic damping coefficients.

		FEM	WADAM/SIMO
Applied at CG	**Surge linear damping: B_{11}**[KN/(m/s)]	75	70
	Heave added mass: A_{33} [t]	1200	1000
	Heave linear damping: B_{33}[KN/(m/s)]	110	110
Applied at the center of each heave plate base	**Heave linear damping: B_{33}**[KN/(m/s)]	76	50
	Heave quadratic damping: B^2_{33}[KN/(m/s)^2]	805	600

Figure 11 shows experimental versus numerical results after calibration for the surge, heave, and pitch decay tests. Good agreement has been reached for the three degrees of freedom. The natural periods obtained by the FEM solver are given in Table 9. Natural periods obtained by the BEM model and experiments are within the round off error of 1 second.

Table 9: Natural periods obtained from decay test with linear restoring.

Surge	**Heave**	**Pitch**
70 s	19 s	26 s

6.3 Catenary mooring

Three catenary lines were used as mooring lines for the rest of the experiments. The location of the end points for each line is given in Table 10. Table 11 provides the mooring line particulars.

Table 10: Mooring lines end points.

	Fairlead point (x,y,z)	**Anchor point (x,y,z)**
Line 1	(-325.73, 0.0, -80.0)	(-23.7318, 0, 10.0027)
Line 2	(206.79, -247.99, -80.0)	(15.24, -18.17, 10.0027)
Line 3	(206.79, 247.99, -80.0)	(15.21, 18.17, 10.0027)

Table 11: Mooring lines particulars.

Length	330 m
Section	$1.108\text{E} \times 10^{-2}\text{m}^2$
Young modulus	5.720×10^{10} Pa
Linear weight in water	1453 N/m

6.4 Validation test 1: monochromatic waves

In this section, Response Amplitude Operators (RAOs) of the computational model presented in this work are compared against those obtained in the experiments. It has to be said that the experimental data shows a change in the platform response along the experiment. In other words, the results of the spectral analysis depend on the time interval used. If the period of time used for calculating the RAOs is chosen towards the end of the experiment, an increase of the response in the low frequencies is observed which has raised the concern on whether longer waves are suitable to be analyzed.

Experimental RAOs were obtained for full scale wave heights of $H = 2$ m and $H = 5$ m, including the elastic lines used for the calibration. The experimental RAO was obtained using a time interval of ten wave cycles, starting at 500 seconds, and using a FFT to filter low frequency components induced by the model basin. The numerical Rao was obtained using a time interval of ten wave cycles, starting at 100 seconds, and using 50 seconds of initialization. Figure 12 compares the RAOs in surge, heave, and pitch, respectively, against the numerical results obtained by the FEM and WADAM/SIMO solvers. While fair agreement is found for the lower periods, the agreement is not so good for the longer ones. This might

be caused by the fact that the distance of the wave generator to the platform is 15.10 meters, while the wavelength range goes from 2.84 m to 26.34 m. Then, longer wave might not have time to fully develop.

6.5 Validation test 2: bichromatic waves

A number of tests were carried out with bichromatic waves in order to analyze the second-order response of the platform. The incident wave periods range between 5.5 and 21 seconds. The wave frequency difference ranges from 0.0128 Hz to 0.0167 Hz. The latter frequency is close, on purpose, to the surge resonant frequency since the focus of the analysis will be on the surge response to the slow drift.

Table 12 provides the experimental test matrix, including incident wave height (H), frequency f, as well as the frequency difference and sum. All these cases have been simulated in the time-domain using the FEM model proposed in this work for the diffraction-radiation problem. The different cases have been analyzed using the quasi-static elastic catenary and the non-linear FEM dynamic cable models. Once the simulations were carried out, the time series have been transformed via Fast Fourier Transform (FFT) to the frequency domain in order to make easier the comparison of the results with the experimental data. No filtering has been made neither to the experimental data, nor to the numerical.

When analyzing the wave elevation of the experiments, it was found that the wave energy spectrum was not as pure bichromatic as expected, showing energy spread around the frequency pair under analysis. Hence in order to better reproduce the experiment, instead of using a pure bichromatic wave, a set of waves reproducing the free surface elevation of the experiment was used.

Figure 13 compares the spectrum of the surge movement obtained in the experiments against the obtained numerically using the FEM solver. Overall, in the range of the incident wave frequencies, the numerical results approximate quite well the experimental ones. However, in the low frequency range, larger differences are appreciated in some cases. Considering the difficulty of even matching the RAOs in the monochromatic wave tests before mentioned, the agreement in the bichromatic wave test is acceptable.

When comparing the quasi-static catenary model against the dynamic cable model, it is observed that both models provide quite similar results, although the catenary model predicts larger movements. This might be due to the lack of energy dissipation of the catenary model itself, while in the dynamic cable model Morison forces in the mooring lines are taken into account, leading to energy dissipation.

Table 13 provides data regarding the CPU time required for simulating the bichromatic wave tests. On average, the ratio of CPU time to real time is in the order of 32.

Table 12: Bichromatic test matrix.

Case	Incident wave 1		Incident wave 2		Freq. difference		Freq. Sum	
	H_1 [m]	f_1 [Hz]	H_2 [m]	f_2 [Hz]	$f_2 - f_1$ [Hz]	T_{diff} [s]	$f_1 + f_2$ [Hz]	T_{sum} [s]
1	5.63	0.0582	4.32	0.0735	0.0153	65.4	0.1318	7.59
2	5.27	0.0667	3.54	0.0813	0.0146	68.3	0.1480	6.76
3	2.80	0.1053	1.62	0.1220	0.0167	59.9	0.2272	4.40
4	2.13	0.1205	1.27	0.1351	0.0147	68.2	0.2556	3.91
5	1.88	0.1300	1.14	0.1429	0.0128	78.0	0.2729	3.66
6	1.50	0.1449	0.92	0.1587	0.0138	72.4	0.3037	3.29
7	1.67	0.1370	1.02	0.1515	0.0145	68.8	0.2885	3.47
8	1.35	0.1515	0.84	0.1667	0.0152	66.0	0.3182	3.14
9	1.22	0.1613	0.77	0.1754	0.0141	70.7	0.3367	2.97
10	1.11	0.1667	0.70	0.1818	0.0152	66.0	0.3485	2.87
11	2.83	0.0909	2.10	0.1053	0.0144	69.7	0.1962	5.10
12	3.37	0.0833	2.44	0.0997	0.0163	61.2	0.1830	5.46
13	4.59	0.0714	3.16	0.0850	0.0135	73.8	0.1564	6.39
14	5.64	0.0526	5.16	0.0672	0.0145	68.9	0.1198	8.35
15	2.82	0.0526	5.16	0.0672	0.0145	68.9	0.1198	8.35
16	3.44	0.0476	6.03	0.0625	0.0149	67.2	0.1101	9.08

Table 13: CPU time for bichromatic wave tests

Case	Catenary mooring			Cable mooring		
	Simulation Time [s]	CPU Time [s]	Ratio [s/s]	Simulation Time [s]	CPU Time [s]	Ratio [s/s]
1	775.02	36227.18	46.74	1200.03	72016.11	60.01
2	1115.14	23947.44	21.47	1115.14	19757.59	17.72
3	1279.19	28688.95	22.43	1279.19	32642.45	25.52
4	1615.12	36035.17	22.31	1615.12	41652.91	25.79
5	1046.01	25104.81	24.00	1046.01	27602.47	26.39
6	935.09	29797.70	31.87	935.09	24044.09	25.71
7	982.07	25378.13	25.84	982.07	25797.82	26.27
8	896.05	30768.33	34.34	896.05	30533.34	34.08
9	854.08	30032.72	35.16	854.08	23306.34	27.29
10	830.08	31300.66	37.71	830.08	38213.82	46.04
11	710.02	53935.90	75.96	710.02	37674.61	53.06
12	1613.07	46106.76	28.58	1613.07	39654.95	24.58
13	1813.12	28062.74	15.48	1813.12	24148.93	13.32
14	1052.09	26884.85	25.55	1052.09	25070.24	23.83
15	1052.09	41201.61	39.16	1052.09	37945.54	36.07
16	836.06	29020.15	34.71	836.06	23880.50	28.56

Mean value			32.58			30.89

6.6 Validation test 3: irregular waves

Two tests in irregular waves are used to validate the capability of the present FEM solver to predict the seakeeping of the HiPRWind, as well as the behavior of the mooring. The simulation time was 784.7 seconds, and the time interval used for the analysis the range between 500 s and 784.7 s. No filtering at all was used along the analysis process, neither to the experimental data, nor to the numerical results. Table 14 provides the particulars of the target wave spectrums. The model discretization used in this test is the same as for the bichromatic tests, but only the cable model is used to simulate the mooring lines.

First of all, the incident wave field was determined by means of a FFT analysis of the incident wave elevation reported by the experiments within the analysis time interval. Figure 14 compares the resulting second order numerical incident wave elevation against the experimental one, finding a good agreement between them.

Figure 15 compares the second-order numerical and experimental surge response within the analysis time interval. A fair agreement is found, although some deviation in the low frequency can be observed. Figure 16 compares the second-order numerical and experimental heave response within the analysis time interval. Again a fair agreement is found, although the numerical solution shows larger amplitudes in the higher frequencies. Figure 17 compares the second-order numerical and experimental pitch response within the analysis time interval. Just like in surge, a fair agreement is found, although some deviation in the low frequency can be observed. Regarding the phase agreement, all movements show a good phase agreement between the numerical and experimental results.

Figure 18 and 19 provide a spectral analysis of the loads induced by the mooring lines on the platform. The numerical results obtained follow well the trend of the experiments, although the amplitude at some frequencies do not match the experimental ones.

Table 14: Irregular wave test matrix.

Case	H_s $[m]$	T_p **[s]**
Irregular 1	2.50	16
Irregular 2	4.00	13

Conclusions

A FEM model for the second-order wave diffraction-radiation problem in the time-domain has been developed. The model has been verified against analytical solutions, comparing mean drift loads for a floating hemisphere, second-order forces for a semi-submerged horizontal rectangular cylinder, and second order forces induced on a bottom mounted cylinder. In all cases, the numerical results obtained are in good agreement with the analytical ones.

Furthermore, the computational solver has been validated against experiments carried out at the ECN Nantes' facilities for the HiPRWind model. In a first stage, the model viscous damping was calibrated to reproduce decay tests for surge, heave, and pitch. A good match between the experiments and the calibrated model was obtained. Then, RAOs were compared using the monochromatic wave tests, finding that the numerical results follow well the experiments for shorter waves, but no for longer waves, probably due to the distance of the platform to the wave maker. Then, surge response of the HiPRWind subject to bichromatic waves were performed and compared to the experiments. Taking into account the experimental uncertainties associated to measuring second-order quantities, it has been found that the computed movements of the platform are in fair agreement with the experimental data. Finally, a validation in irregular waves under two different condition was carried out. Again, the up to second-order movements amplitudes predicted numerically were compared with the experiments, showing a good phase agreement, and a fair agreement in amplitude.

Regarding the modeling of the mooring lines, the obtained results in bichromatic waves agree well with the experimental trends. They also indicate that both, the quasi-static catenary model and the nonlinear FEM dynamic cable, provide quite similar results. In irregular waves, the loads induced by the dynamic cable on the structure show a similar pattern than the experimental results. They show a quite fair agreement in the order of magnitude of the loads obtained, and a similar trend across frequencies.

In conclusion, the second-order time-domain FEM model presented in this work, along with the mooring models used, have good alternative capabilities to solve the second-order seakeeping of floating platforms.

Acknowledgements

The authors acknowledge ECN Nantes which facilities (used under the EU MARINET program) made this work possible.

The authors thank Acciona Energía and Fraunhofer Institute, and especially to Raul Manzanas, for providing the data regarding the FP7 project HiPRWind, and the “Universidad Politécnica de Madrid” for granting access to EU MARINET SEMISO project experimental results.

Thanks to Carlos Lopez Pavon for providing the numerical results obtained with WADAM/SIMO and show in this work.

The research leading to these results has received funding from the Spanish Ministry for Economy and Competitiveness under Grants ENE2014-59194-C2-1-R and ENE2014-59194-C2-2-R (X-SHEAKS).

The authors also gratefully acknowledge the support of NVIDIA Corporation with the donation of a TeslaK20 GPU used for this research.

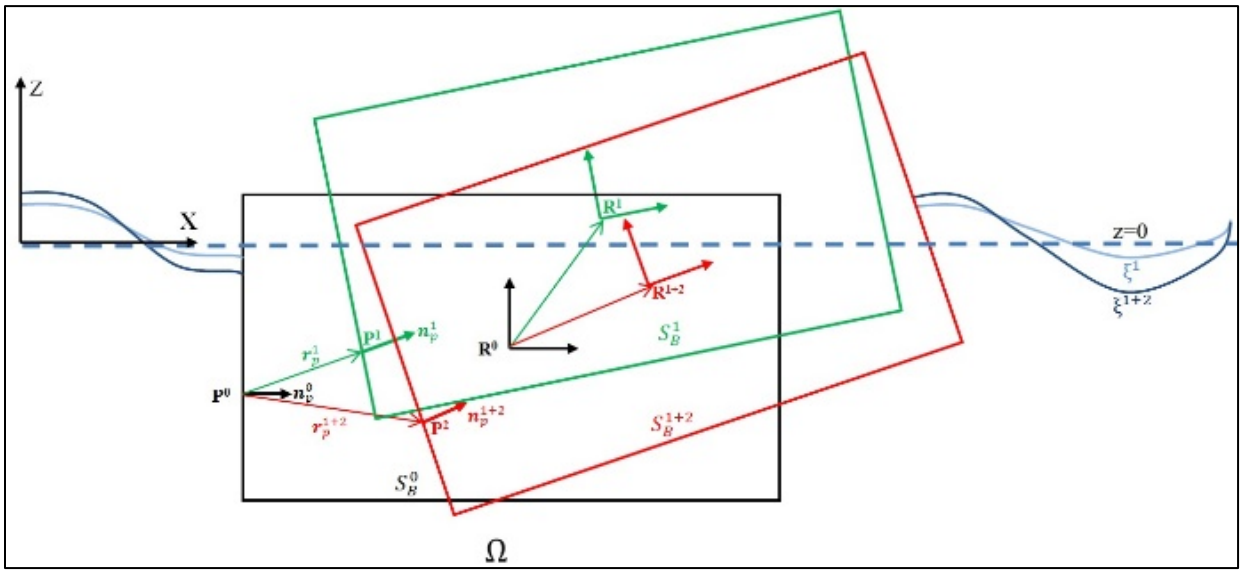

Figure 1: First and second-order rigid body movement.

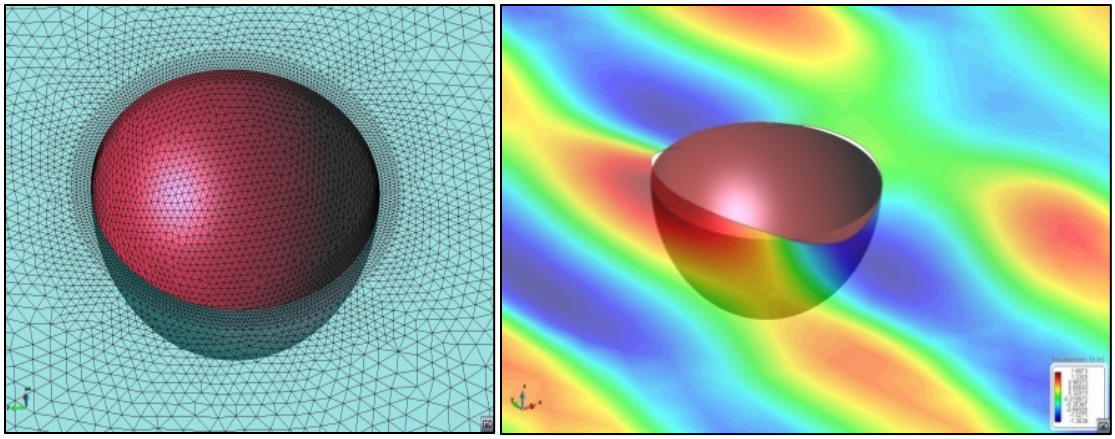

Figure 2: Hemisphere: mesh refinement close up (left) and wave contours (right).

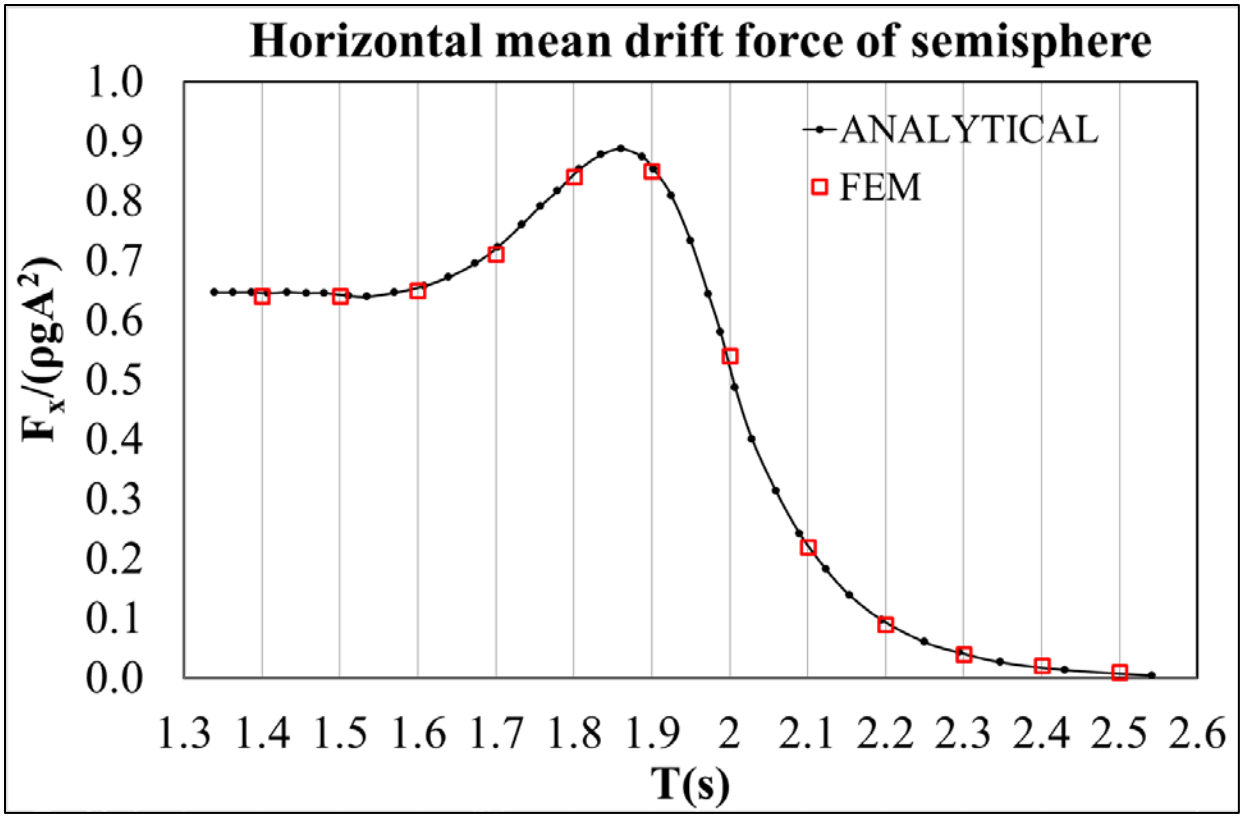

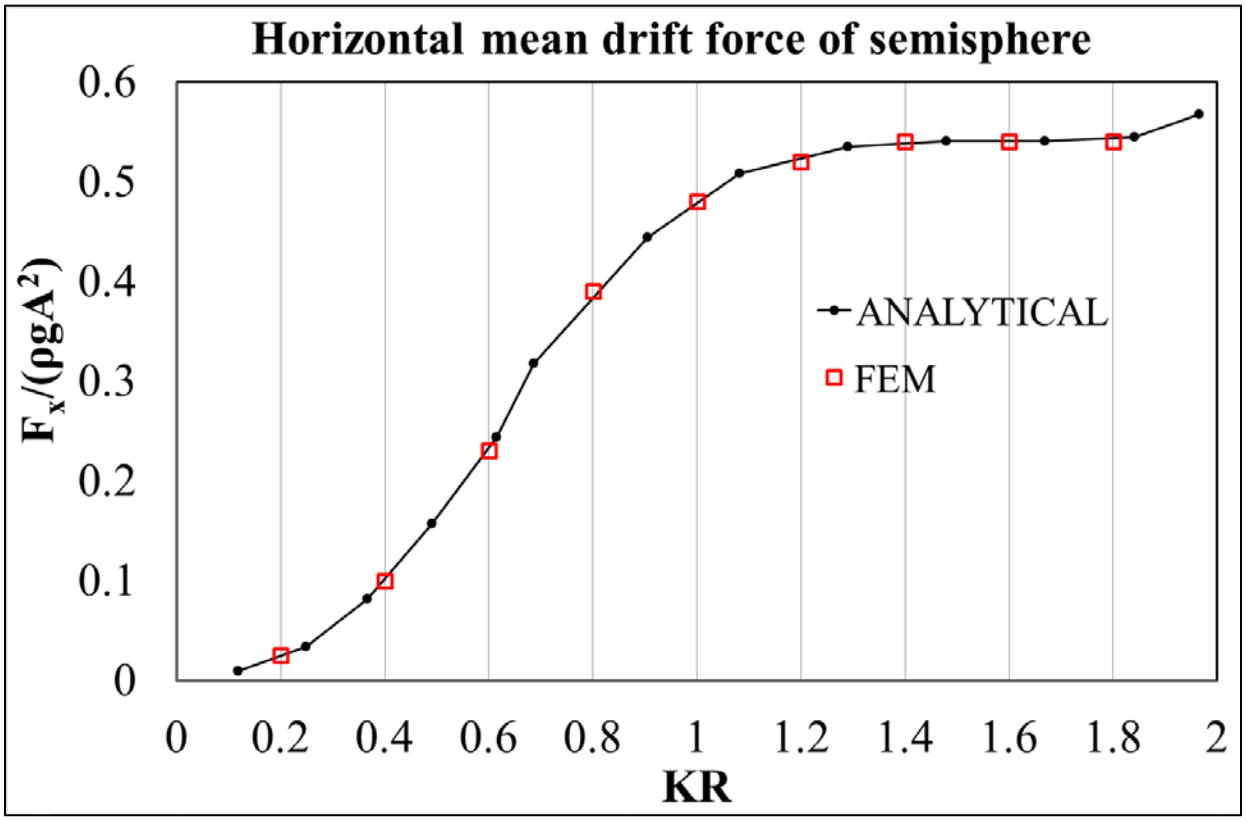

Figure 3: Mean drift forces on Hemisphere.

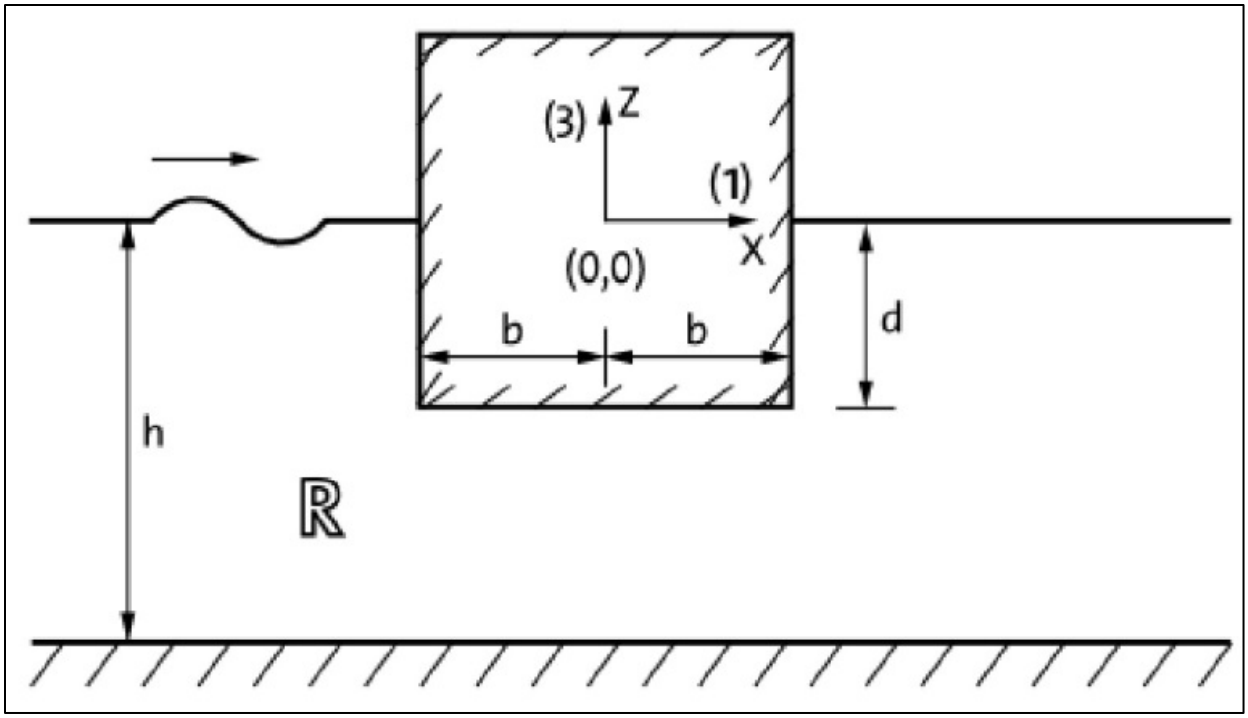

Figure 4: Horizontal semi-submerged cylinder: problem layout.

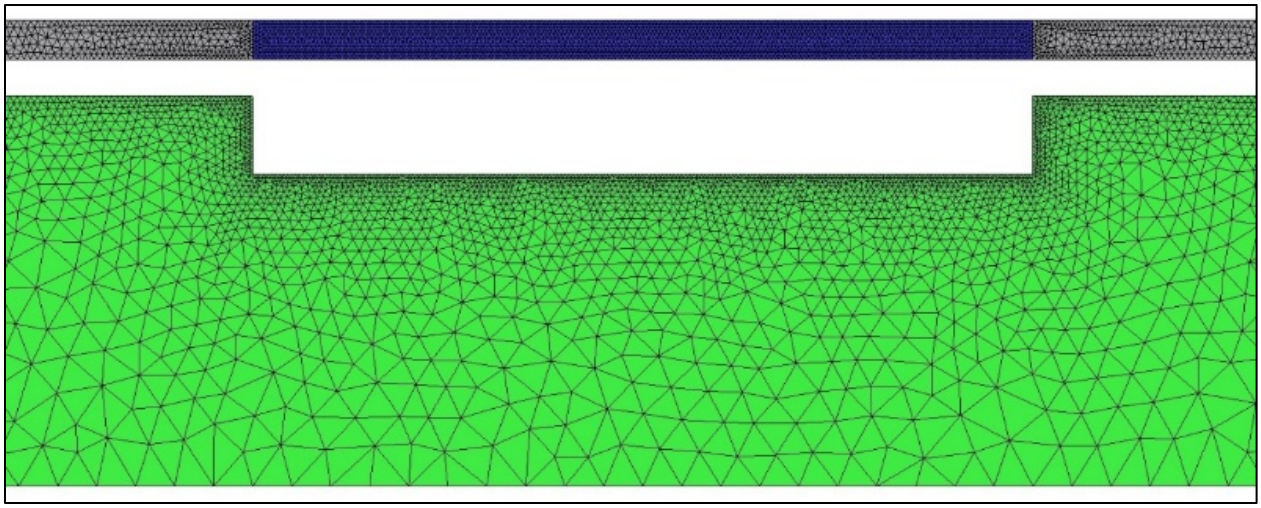

Figure 5: Generated mesh: Top view (up) and front view (down).

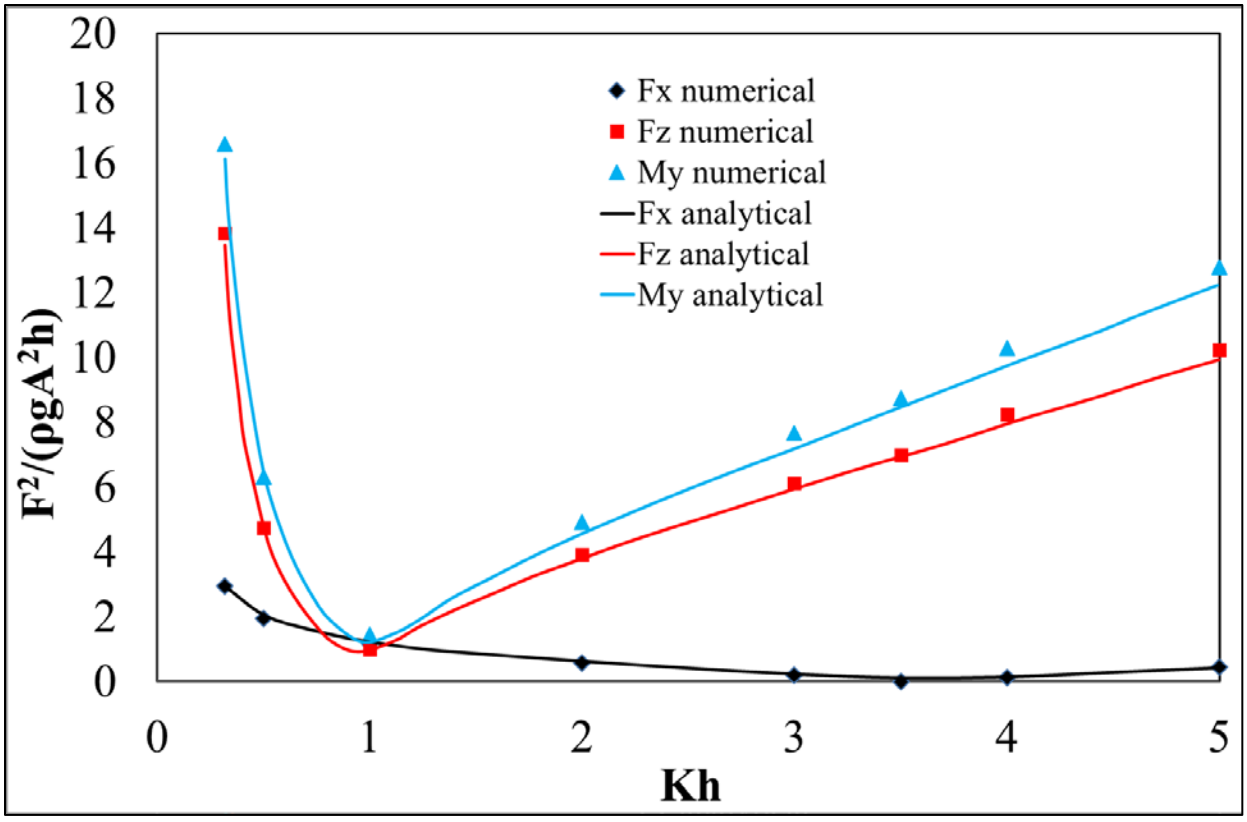

Figure 6: Second-order wave forces on a rectangular cylinder: analytical versus numerical.

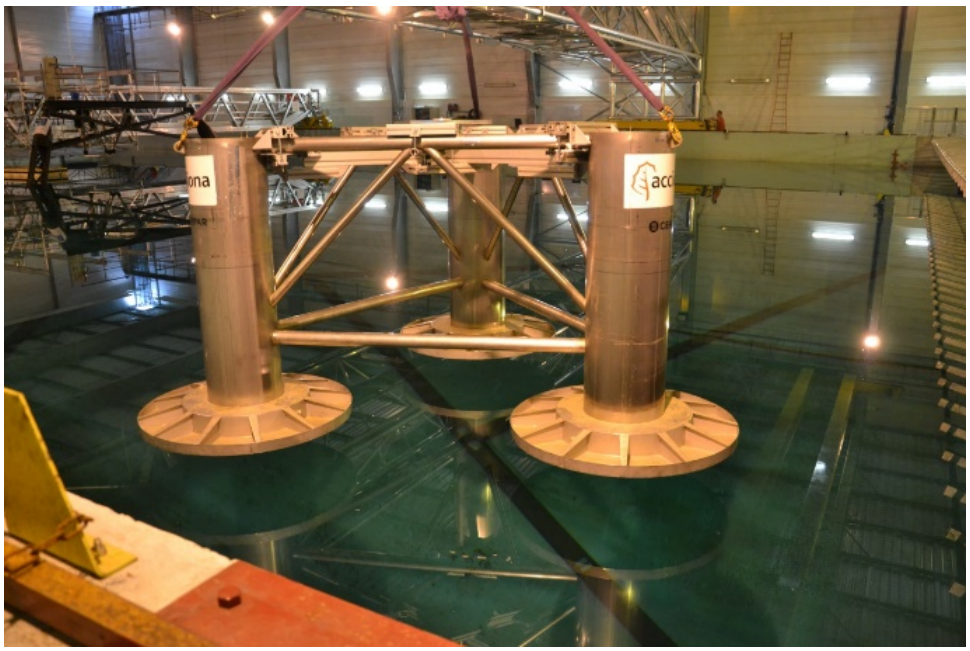

Figure 7: HiPRWind platform model used.

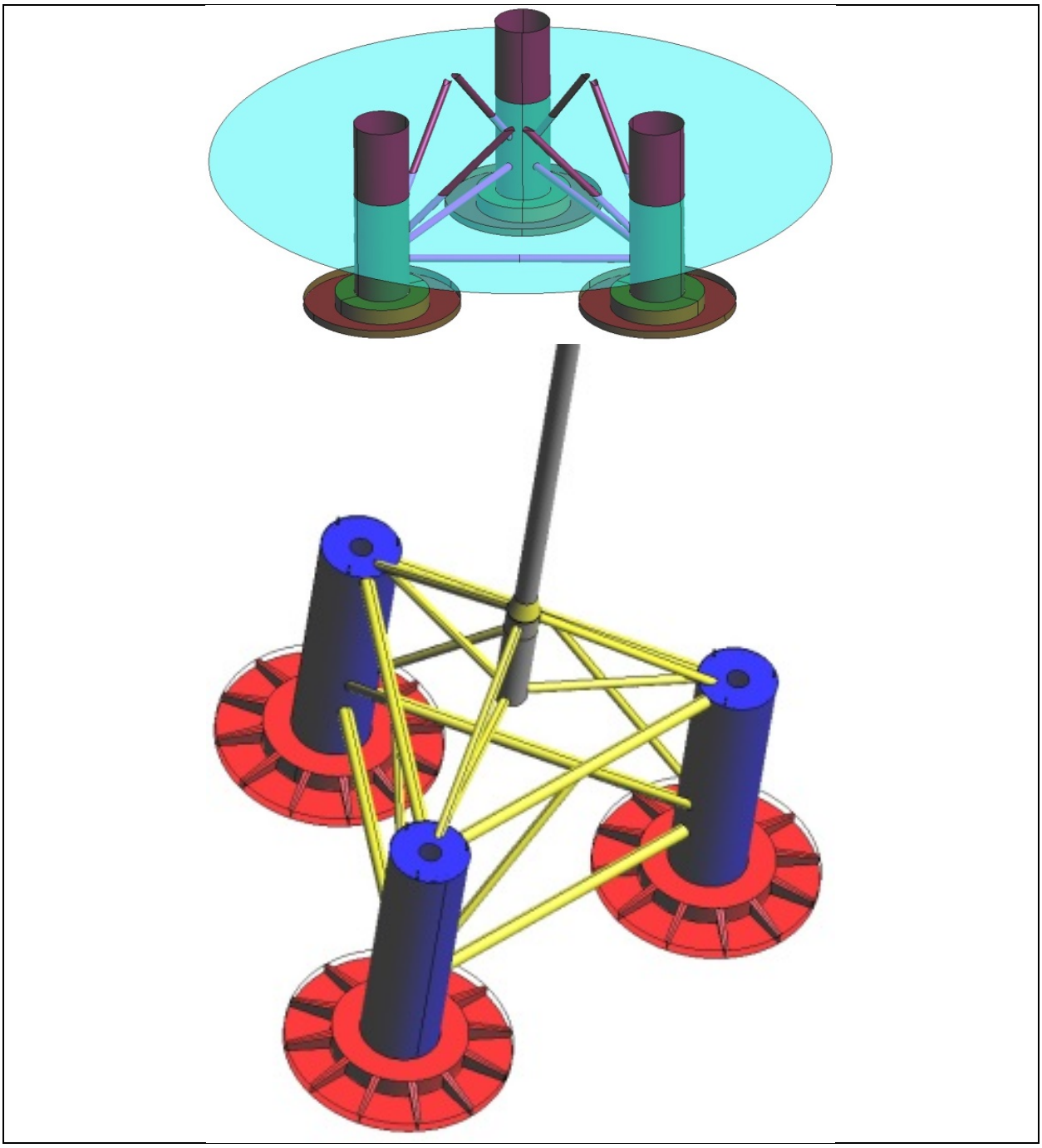

Figure 8: HiPRWind computational model overview.

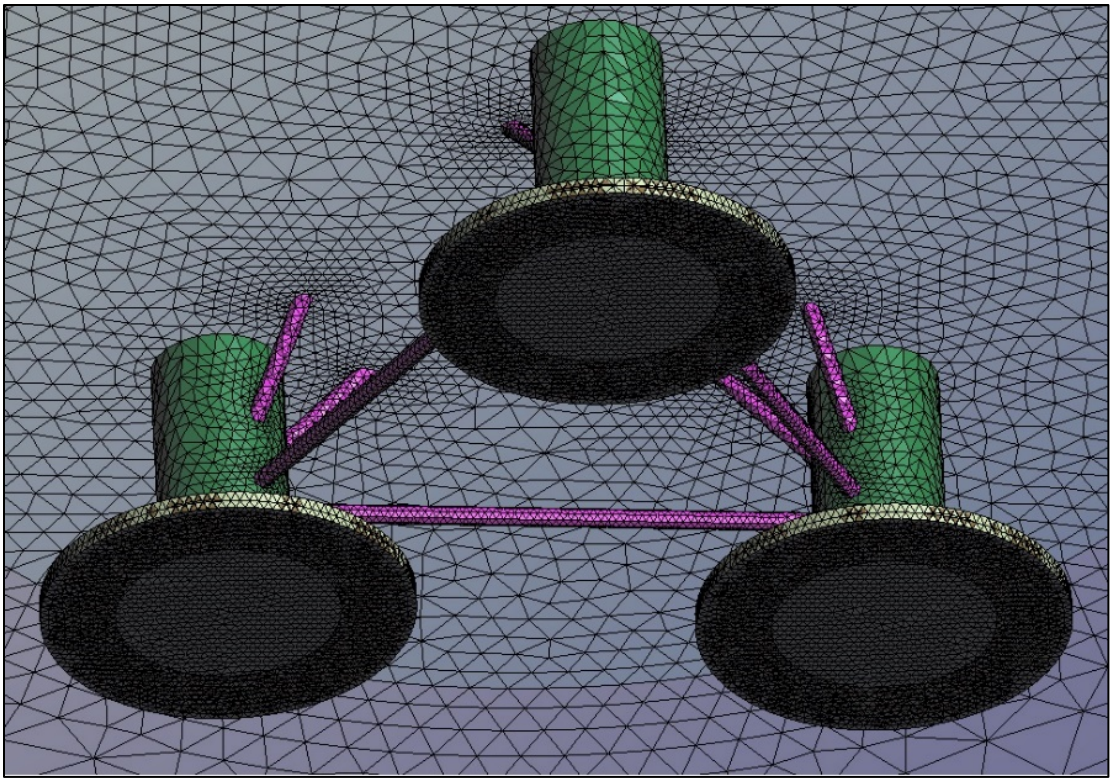

Figure 9: FEM model mesh.

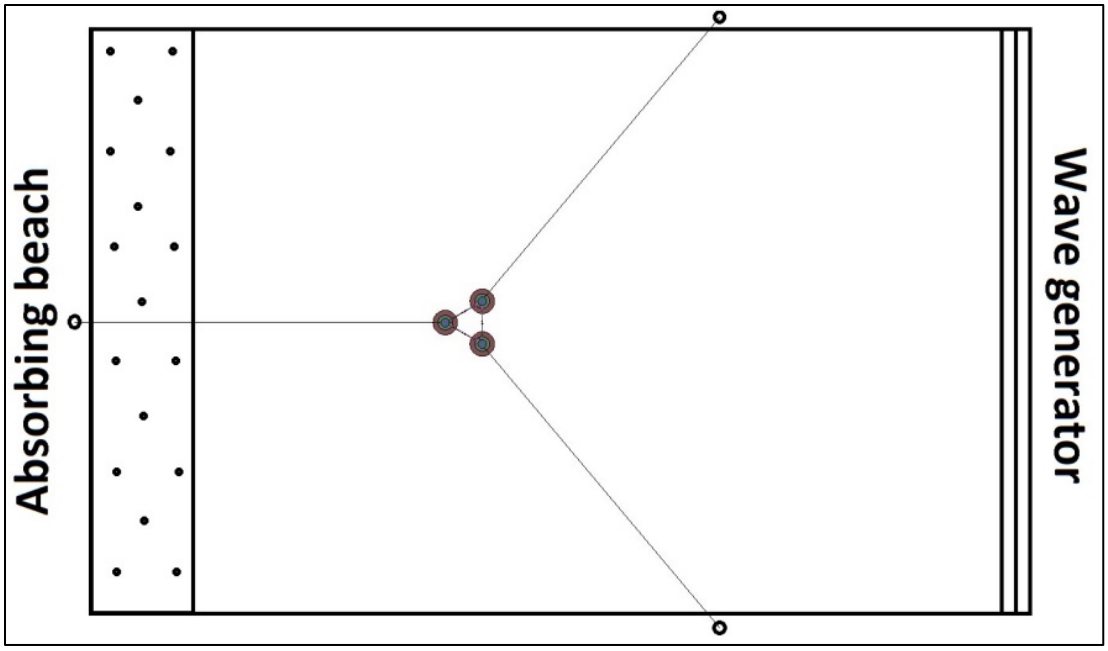

Figure 10: Model basin setup including elastic mooring.

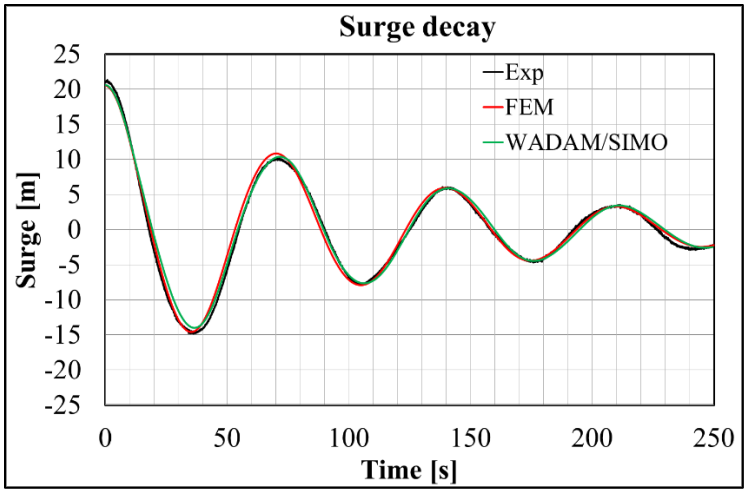

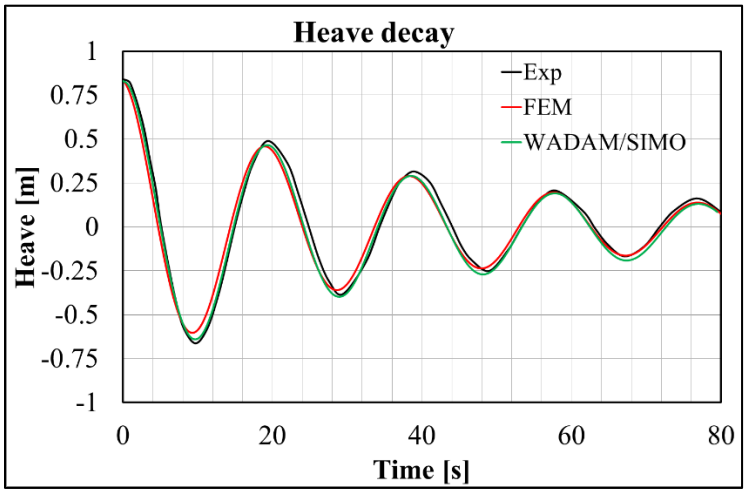

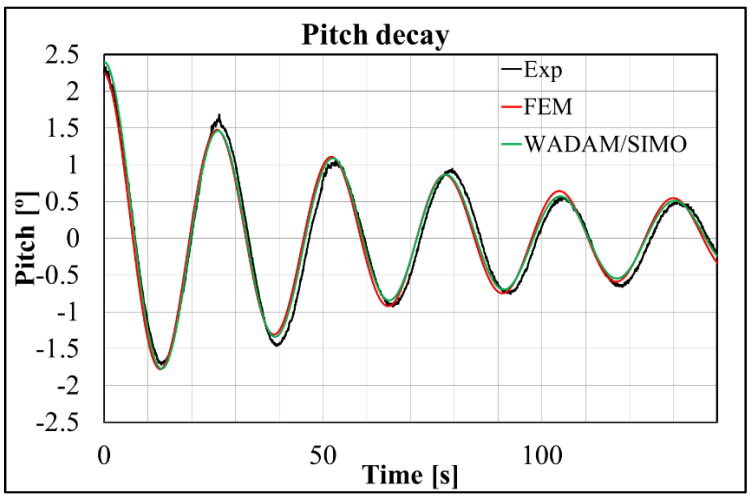

Figure 11: Comparison between experimental and numerical decay tests.

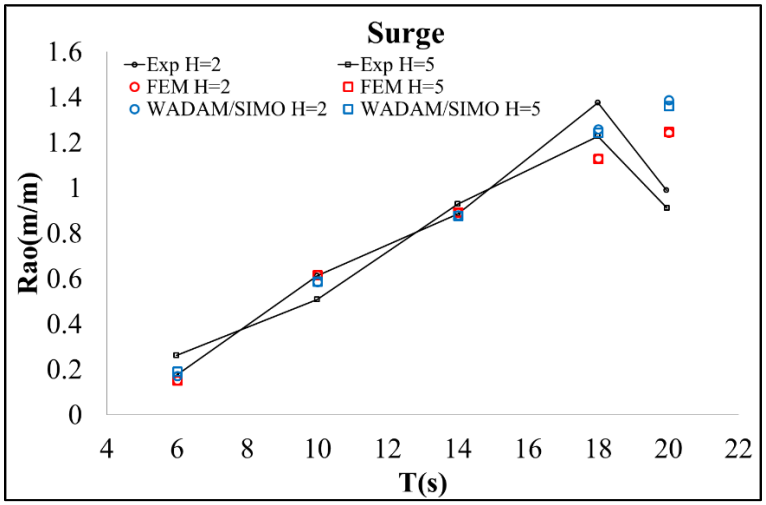

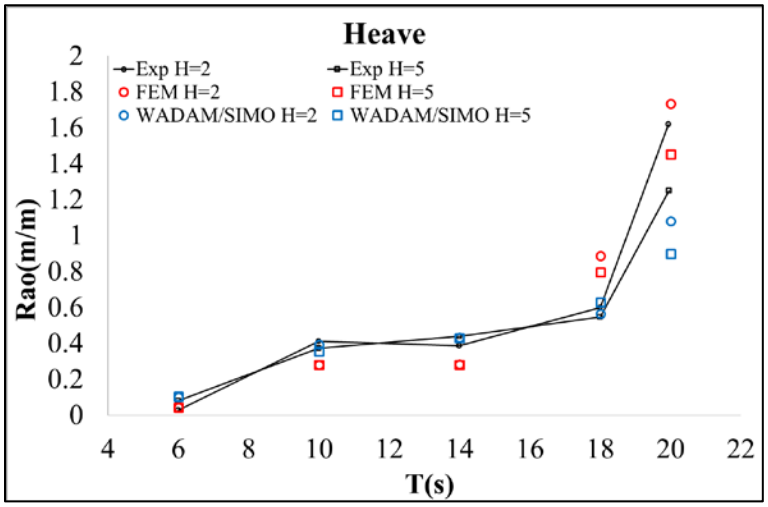

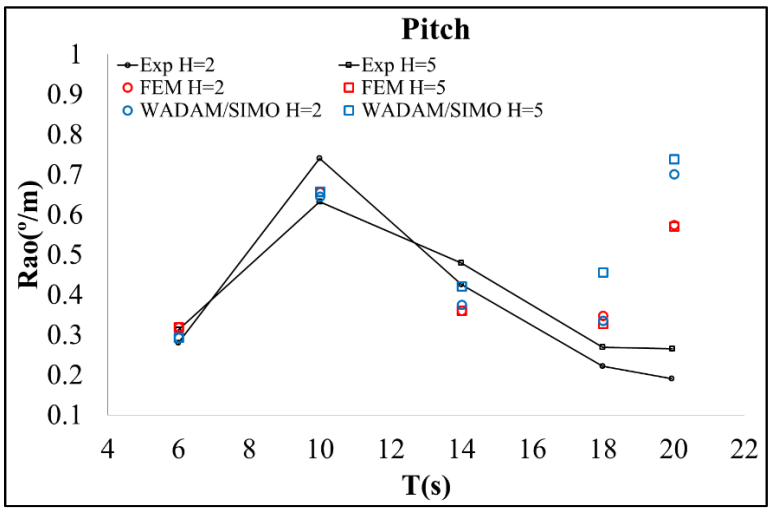

Figure 12: Comparison of RAOs obtained from experiments and numerical simulations.

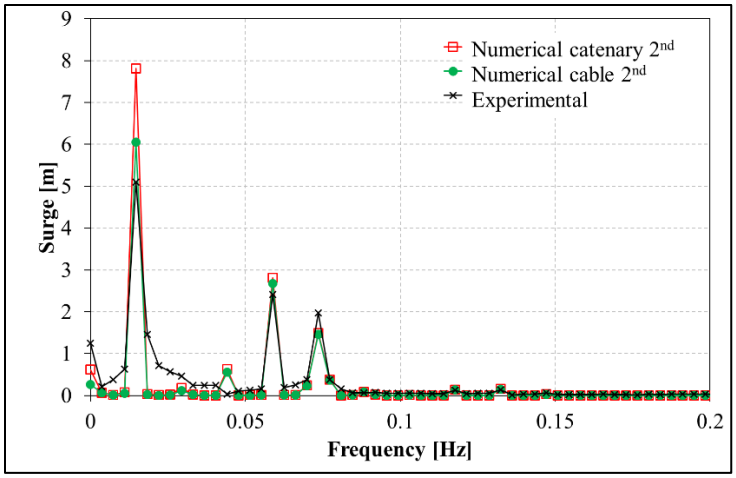

(a): Case 1

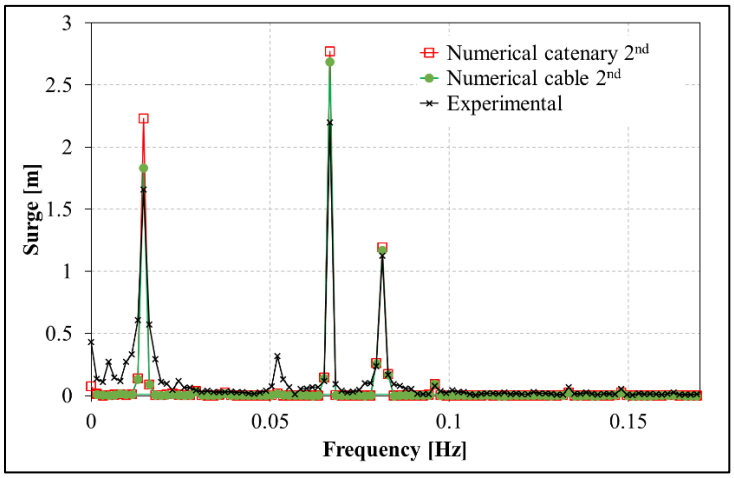

(b): Case 2

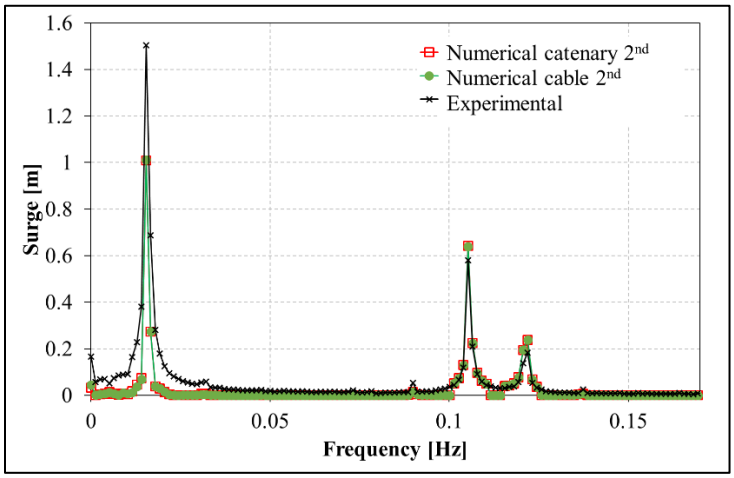

(c): Case 3

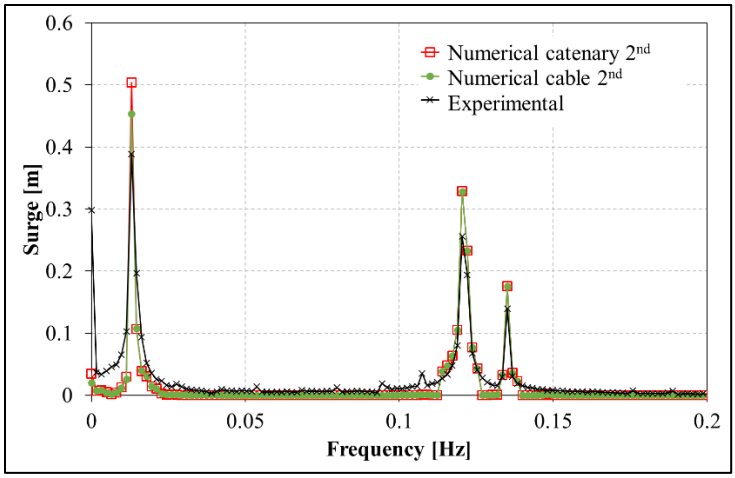

(d): Case 4

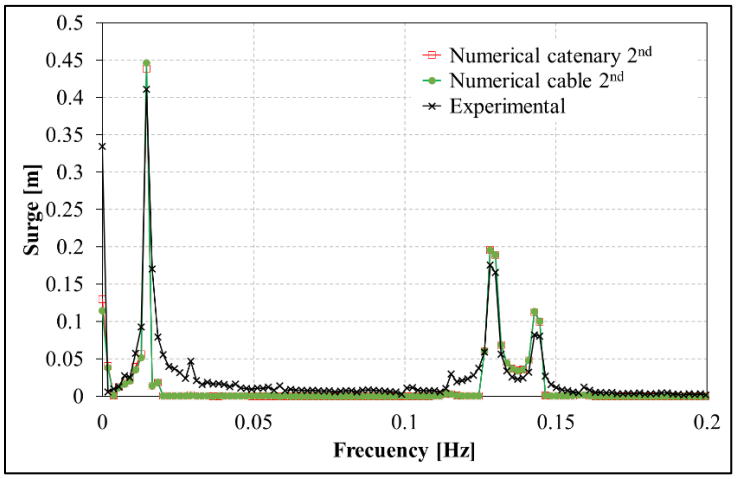

(e): Case 5

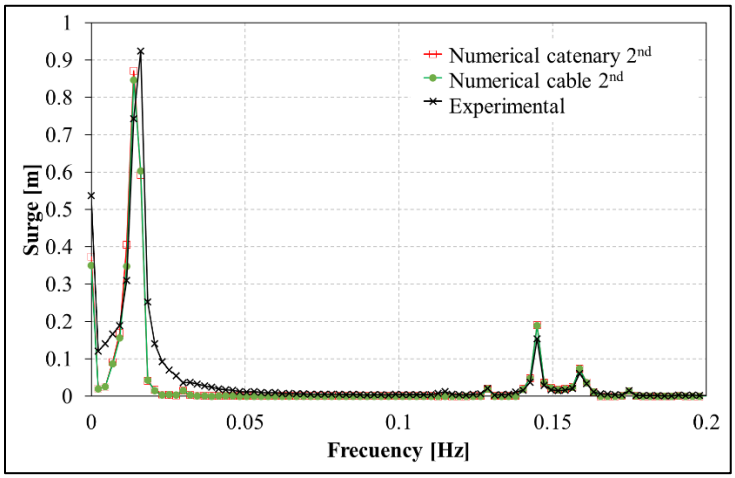

(f): Case 6

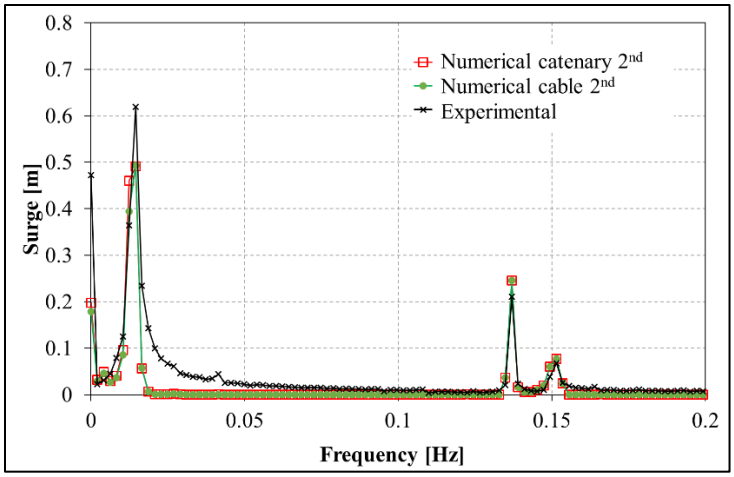

(g): Case 7

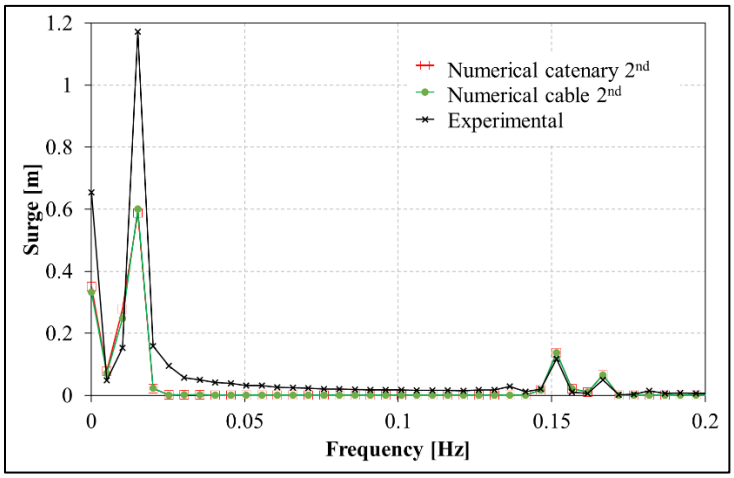

(h): Case 8

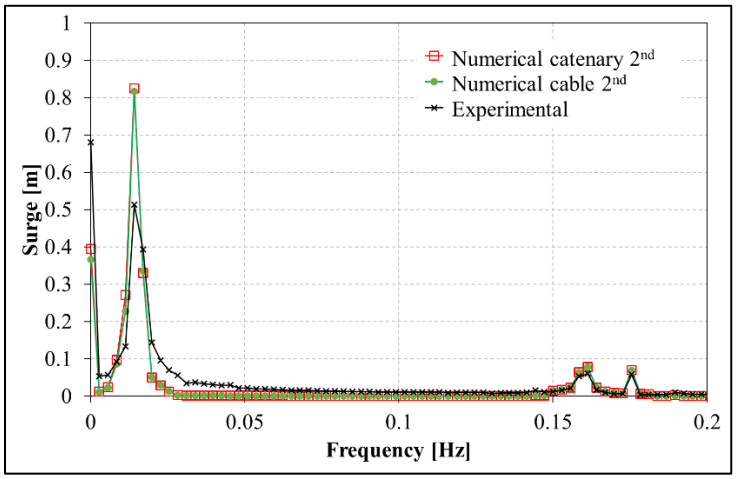

(i): Case 9

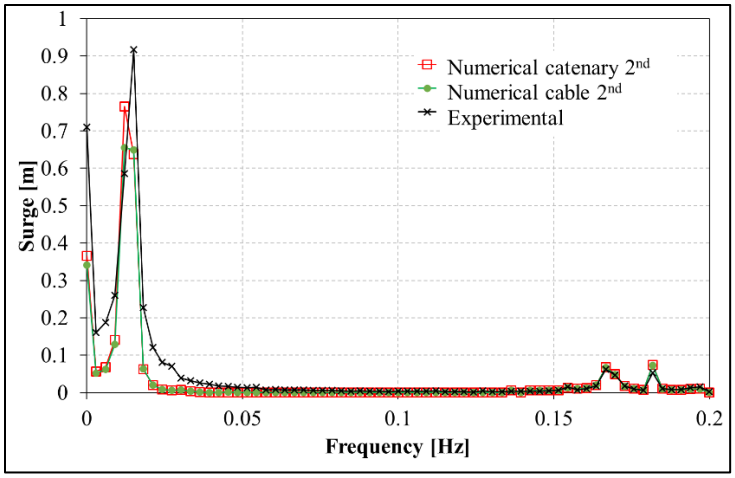

(j): Case 10

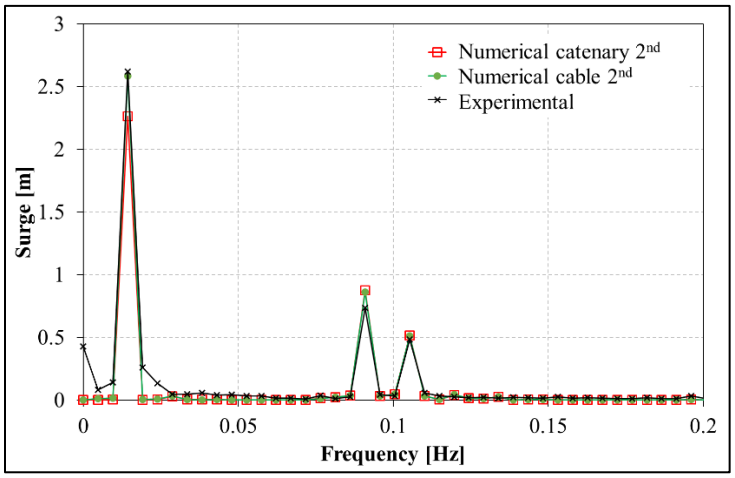

(k): Case 11

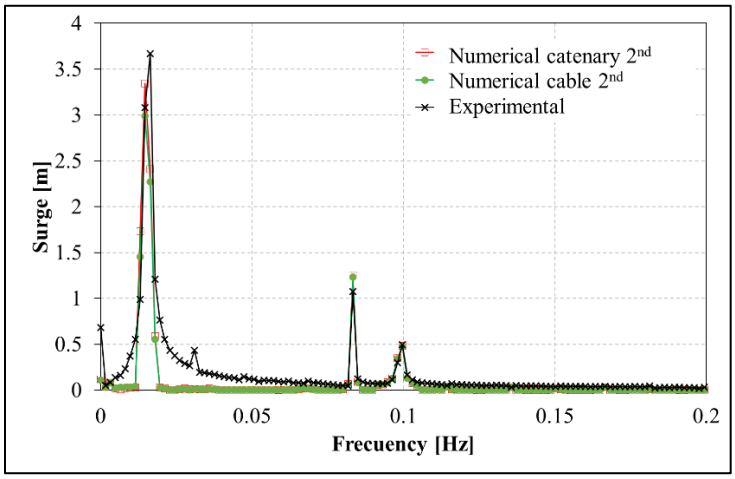

(l): Case 12

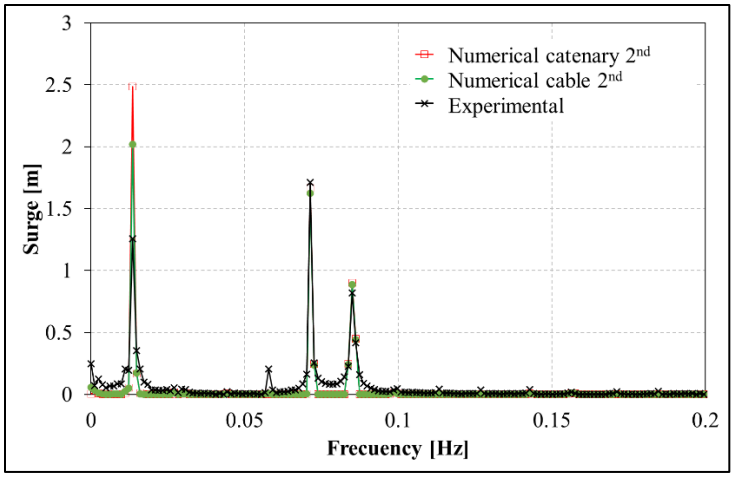

(m): Case 13

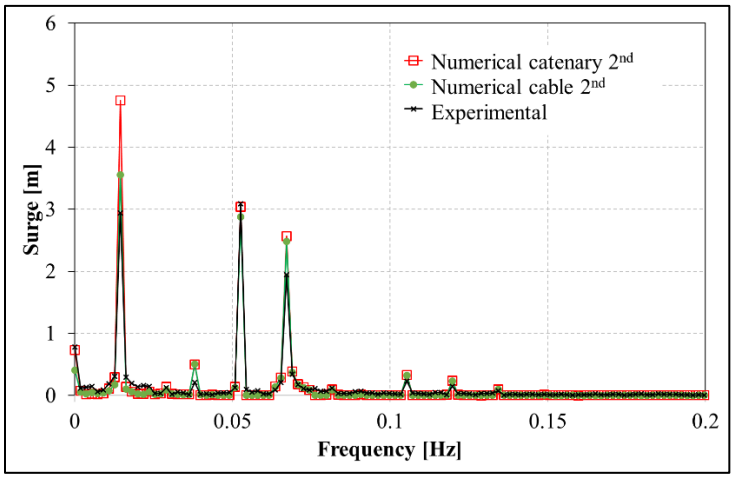

(n): Case 14

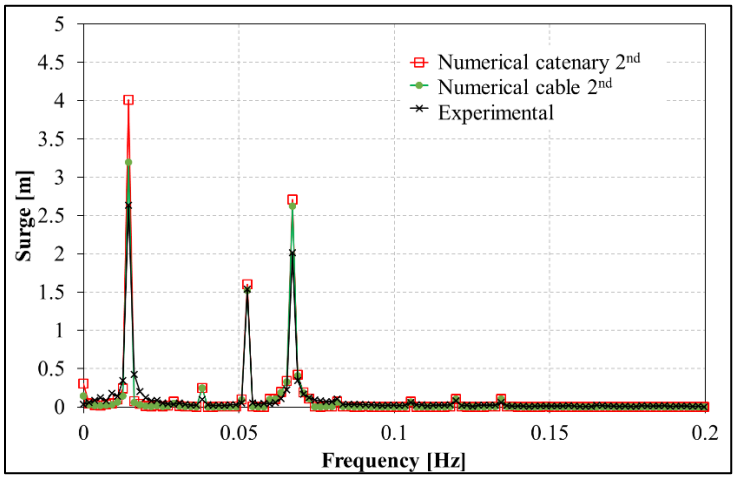

(o): Case 15

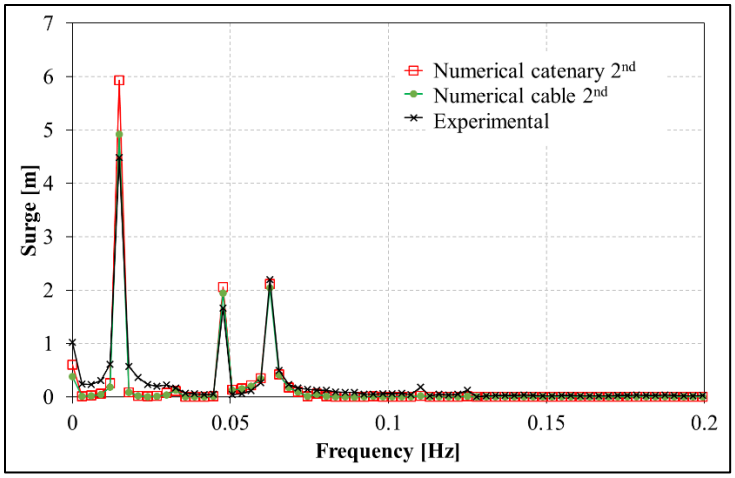

(p): Case 16

Figure 13 (a)-(p): Comparison between the experimental, catenary and cable model for surge response to bichromatic waves.

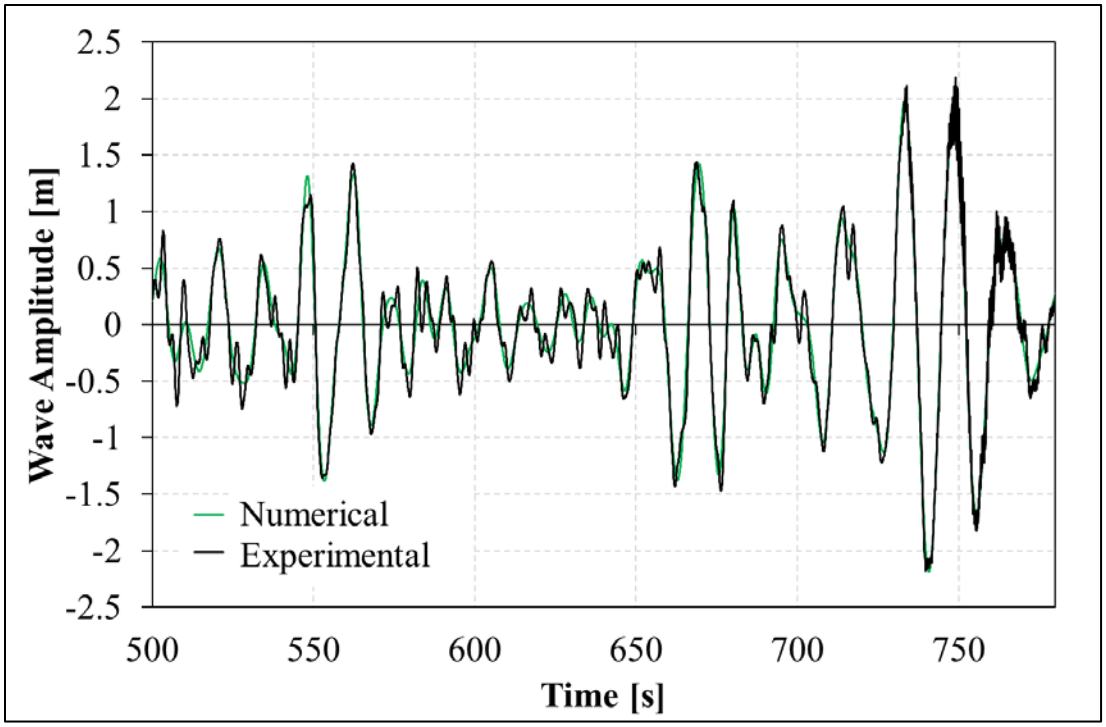

1

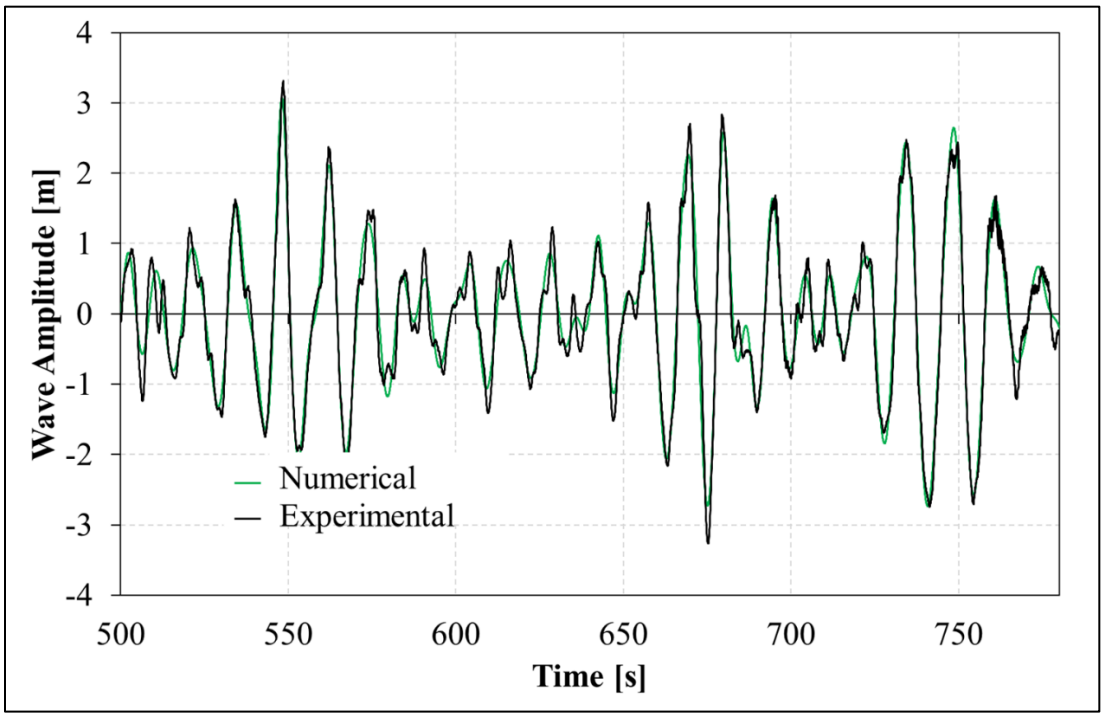

2

3 Figure 14: Comparison between experimental and second order numerical incident wave elevation for the time
4 range analyzed. Up: Irregular 1; down: Irregular 2.

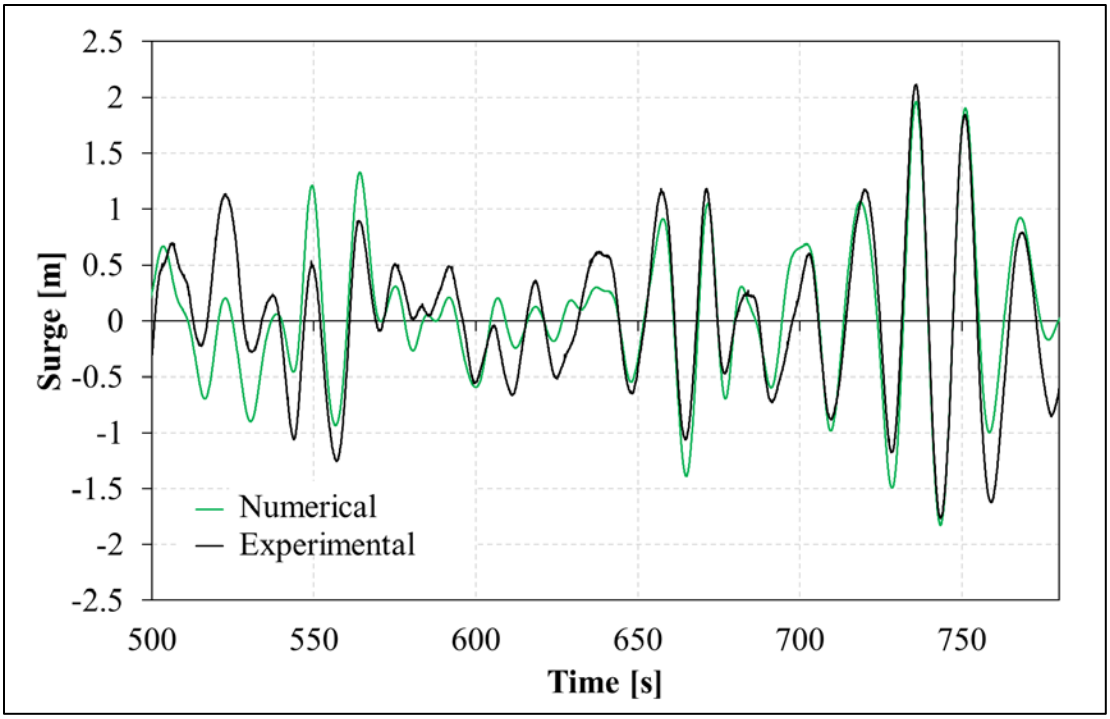

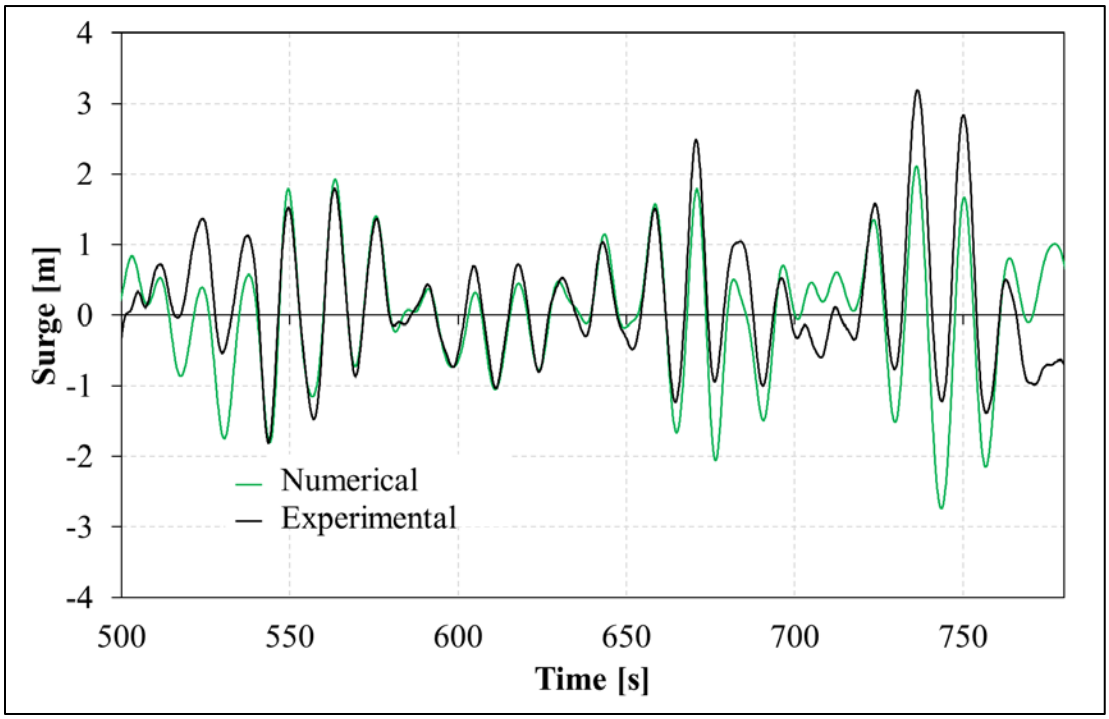

Figure 15: Comparison between experimental and second order numerical surge movements for the time range analyzed. Up: Irregular 1; down: Irregular 2.

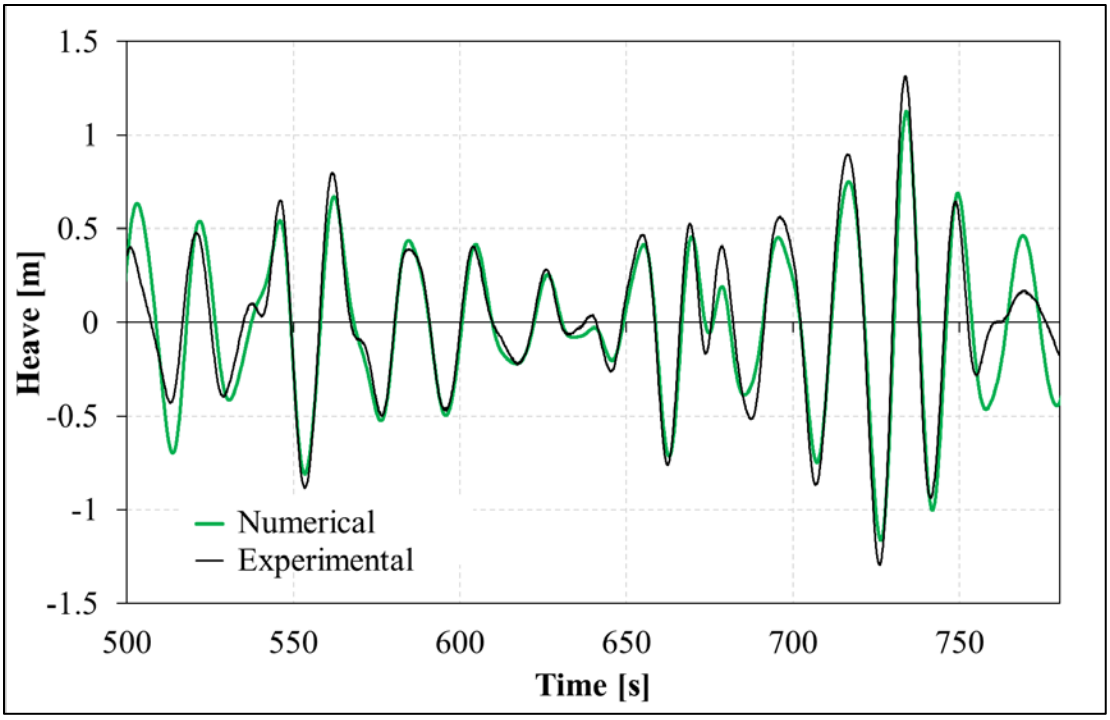

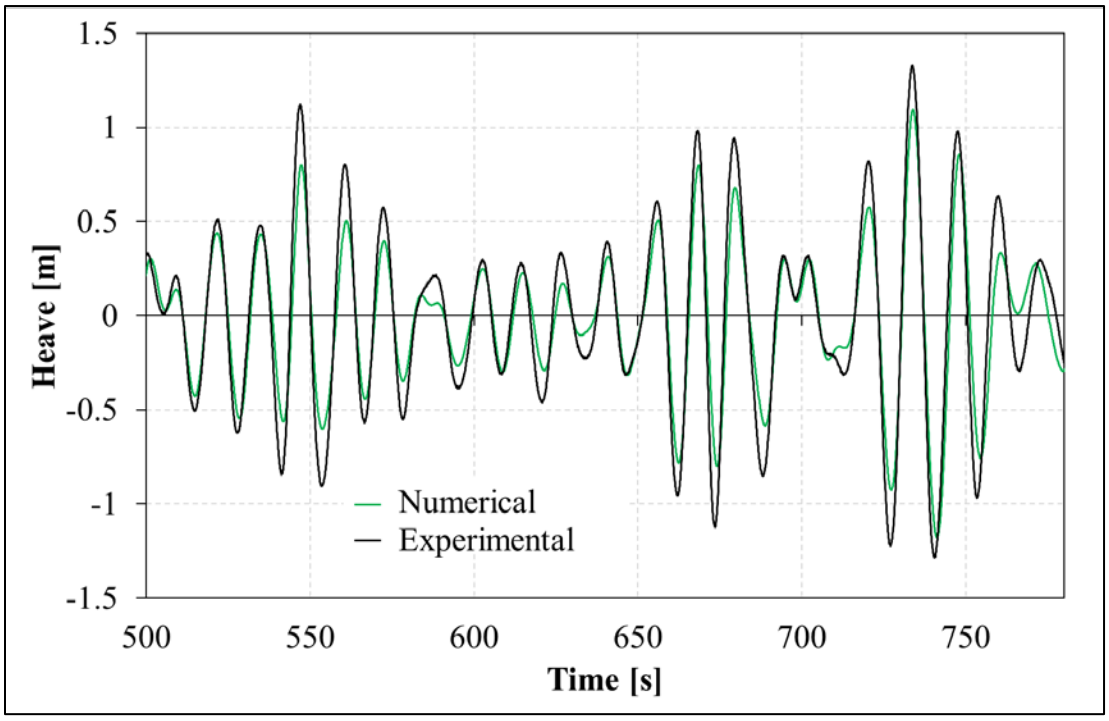

Figure 16: Comparison between experimental and second order numerical heave movements for the time range analyzed. Up: Irregular 1; down: Irregular 2.

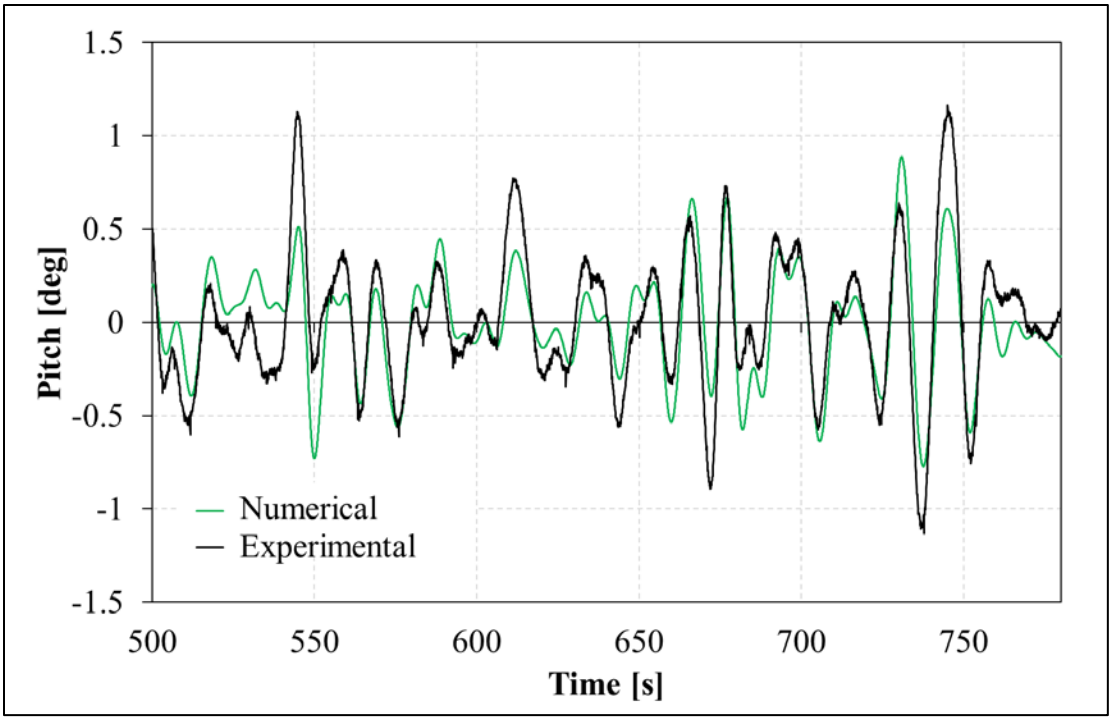

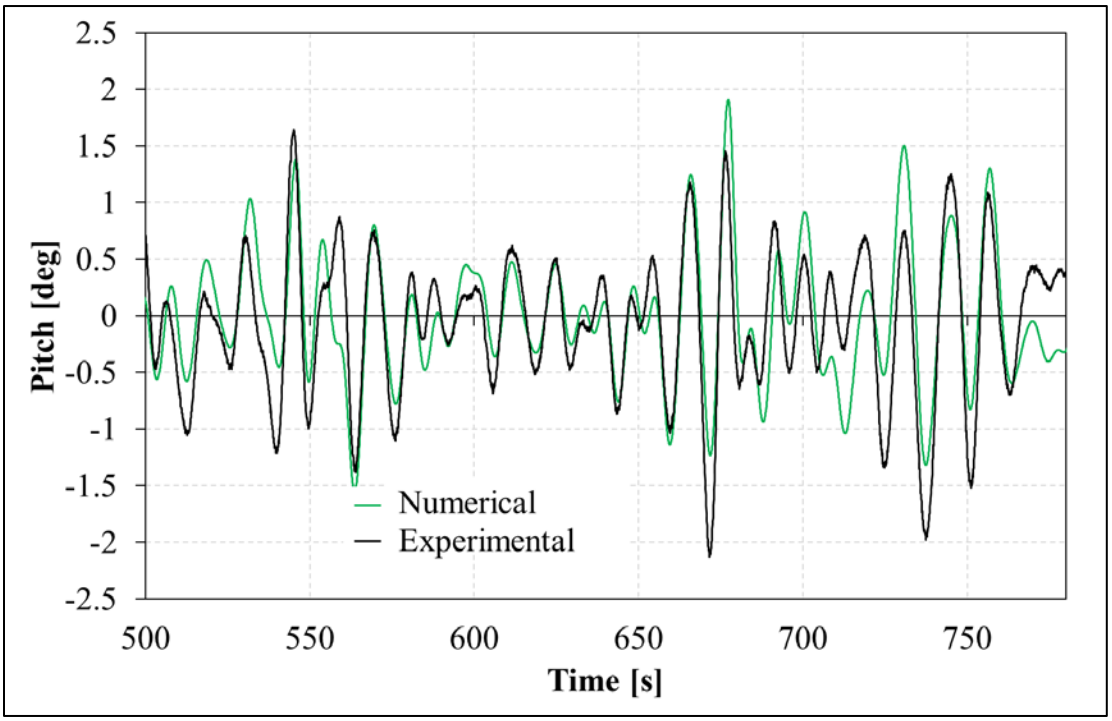

Figure 17: Comparison between experimental and second order numerical pitch movements for the time range analyzed. Up: Irregular 1; down: Irregular 2.

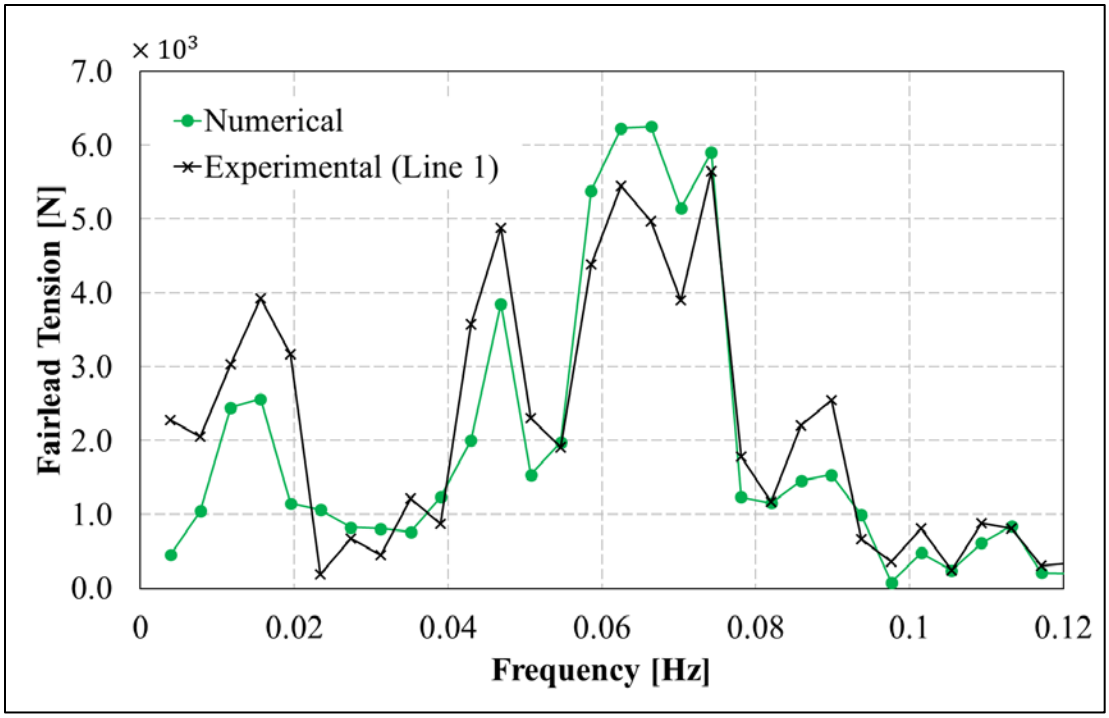

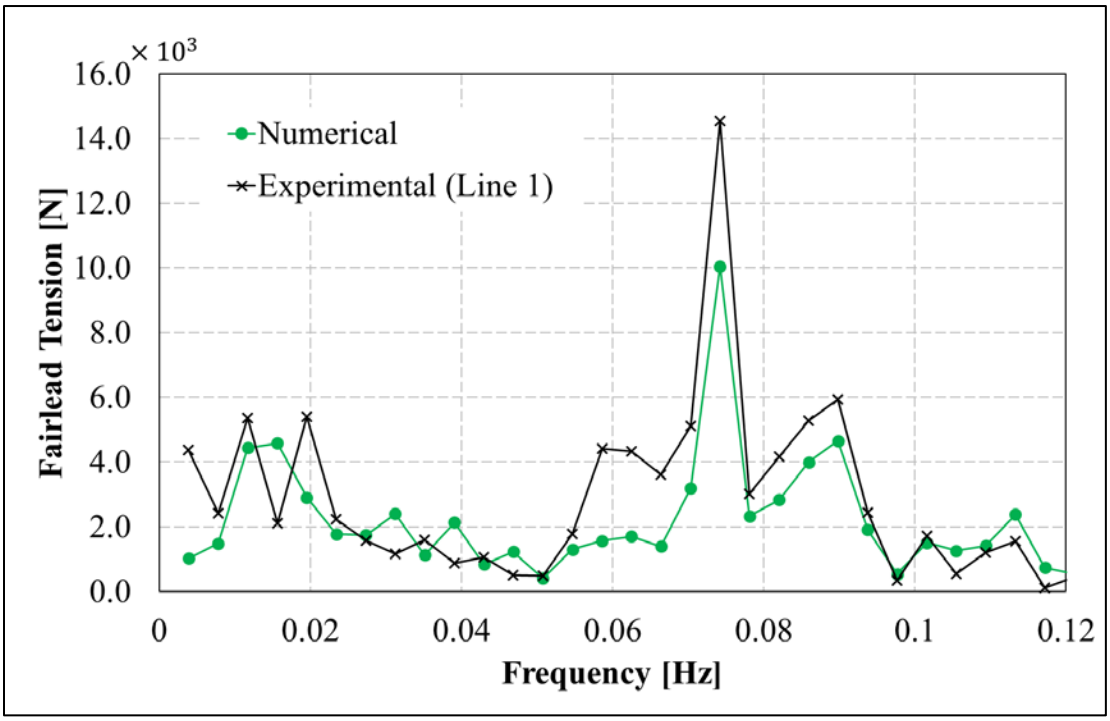

Figure 18: Comparison between experimental and second order numerical line 1 loads in the frequency domain. Up: Irregular 1; down: Irregular 2.

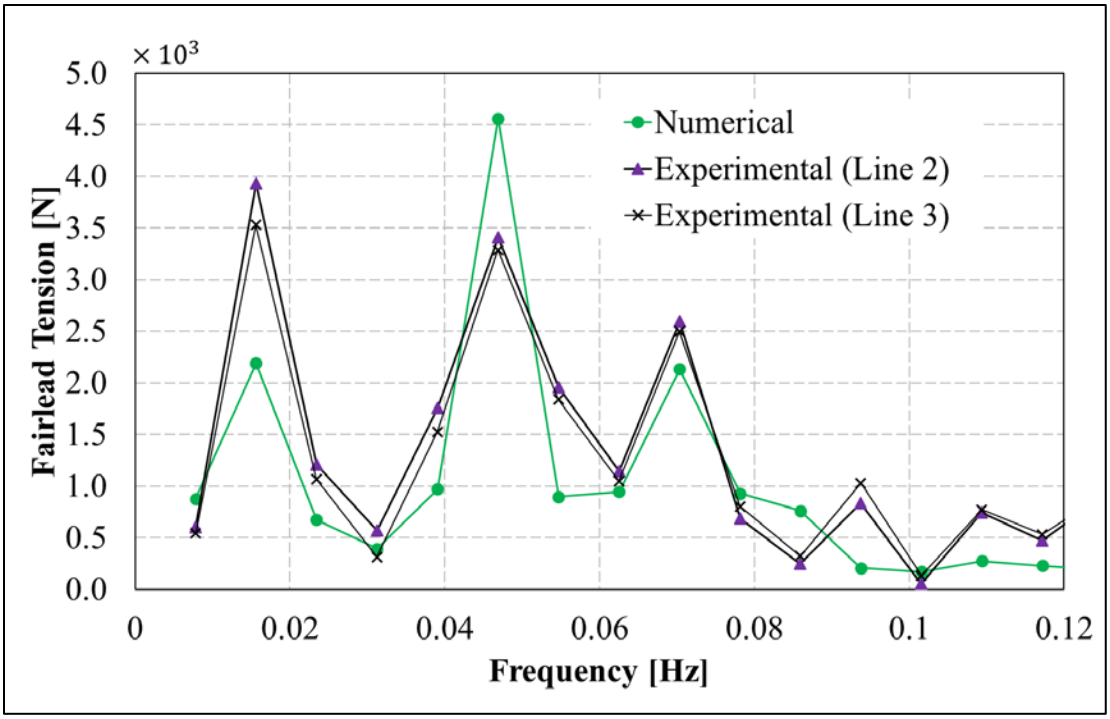

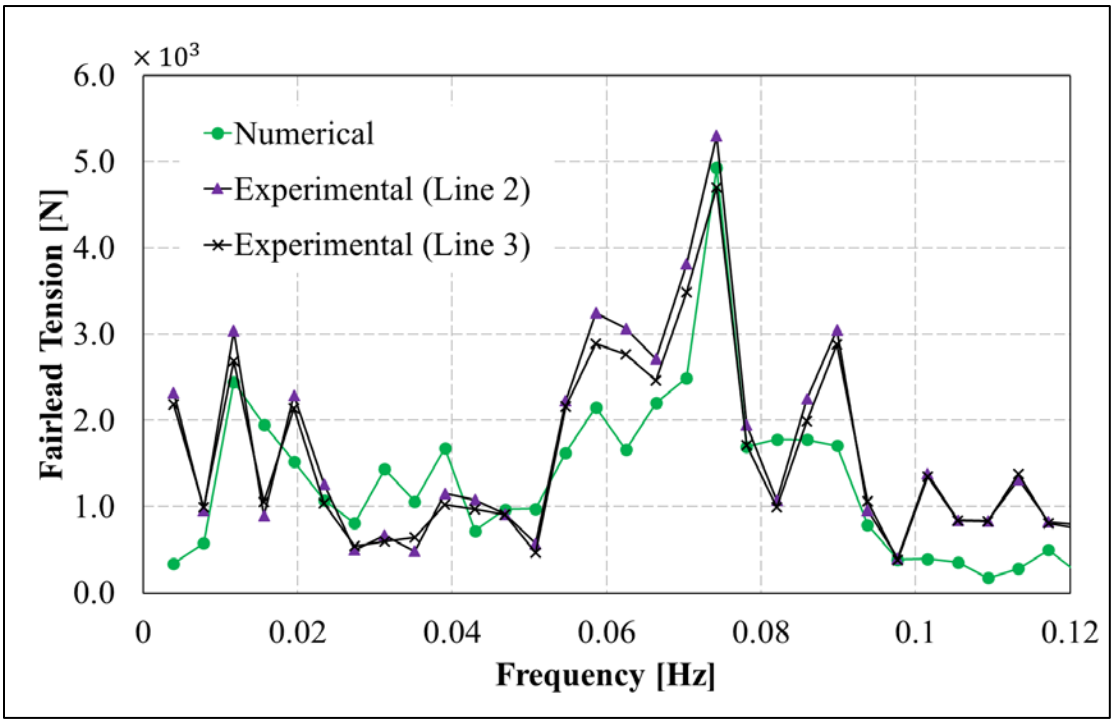

Figure 19: Comparison between experimental and second order numerical line 1 loads in the frequency domain. Up: Irregular 1; down: Irregular 2.

References

[1] Hanson, T. D., Skaare, B., Yttervik, R., Nielsen, F. G. and Havmoller, O., 2011, “Comparison of Measured and Simulated Responses at the First Full Scale Floating Wind Turbine HYWIND,” Presented at EWEA 2011, European Wind Energy Association, Brussels, Belgium

[2] Roddier, D., Cermelli, C., Aubault, A. and Weinstein, A. “Windfloat: A Floating Foundation for Offshore Wind Turbines,” J. Renewable Sustainable Energy 2010, 2(3), p. 033104.

[3] Maine International Consulting LLC, 2012, “Floating Offshore Wind Foundations: Industry Consortia and Projects in the United States, Europe and Japan,” Overview Report, Bremen ME.

[4] Breton S.P. and Moe H. Status, plans and technologies for offshore wind turbines in Europe and North America. Renew Energy 2009; 34:646-54.

[5] Strach-Sonsalla M. and Muskulus M. Prospects of Floating Wind Energy, International Journal of Offshore and Polar Engineering, 2016. 26:81-87.

[6] Lupton, R.C. and Langley, R.S. Scaling of slow-drift motion with platform size and its importance for floating wind turbines. Renewable Energy 2017; 101: 1013e1020.

[7] Lopez-Pavon, C., Watai, R. A., Ruggeri, F., Simos, A. N. and Souto-Iglesias, A. Influence of Wave Induced Second-Order Forces in Semisubmersible FOWT Mooring Design. Journal of Offshore Mechanics and Arctic Engineering 2015; 137 / 031602-1.

[8] Peiffer, A., Aubault, A. and Weinstein, J., 2011, “A Generic 5 MW Windfloat for Numerical Tool Validation & Comparison Against a Generic Spar,” ASME Paper No. OMAE2011-50278.

[9] Liu, Y., Li, S., Yi, Q. and Chen, D. Developments in semi-submersible floating foundations supporting wind turbines: A comprehensive review. Renewable and Sustainable Energy Reviews 2016; 60:433–449.

[10] Liua M., Xiaoa, L., Lua, H. and Shia J. Experimental investigation into the influences of pontoon and column configuration on vortex-induced motions of deep-draft semi-submersibles. Ocean Engineering 2016; 123: 262–277.

[11] Philippe, M., Babarit, A. and Ferrant, P. Aero-Hydro-Elastic Simulation of a Semi-Submersible Floating Wind Turbine. ASME Paper No. OMAE2012-84070.

[12] Coulling, J.A., Goupee, J.A., Robertson A.N. and Jonkman, J.M. Importance of Second-order difference wave diffraction forces in the validation of FAST semi-submersible floating wind turbine model. ASME 2013 32nd International Conference on Ocean, Offshore and Arctic Engineering Nantes, France June 9-14, 2013.

[13] Bayati, I., Joknman, J., Robertson, A. and Platt, A. The effects of second-order hydrodynamics on a semisubmersible floating offshore wind turbine. Journal of Physics: Conference Series 524 (2014) 012094 doi:10.1088/1742-6596/524/1/012094.

[14] Matos, V.L.F, Simos, A.N. and Sphaier, S.H. Second-order resonant heave, roll and pitch motions of a deep-draft semi-submersible: Theoretical and experimental results. Ocean Engineering 2011. 38: 2227–2243.

[15] Simos,A.N., Ruggeri, F., Watai, R., Souto-Iglesias, A., and Lopez-Pavon, C. Slow-drift of a Floating Wind Turbine: An Assessment of Frequency-Domain Methods based on Model Tests (submitted for publication).

[16] Servan-Camas, B. and García-Espinosa, J. Accelerated 3D multi-body seakeeping simulations using unstructured finite elements. J Comput Phys 2013; 252:382e403.

[17] Servan-Camas, B. A time-domain finite element method for seakeeping and wave resistance problems. School of Naval Architecture and Ocean Engineering, Technical University of Madrid; 2016 [Doctoral thesis]. http://oa.upm.es/39794/1/BORJA_SERVAN_CAMAS.pdf

[18] Gutiérrez-Romero, J.E., Serván-Camas, B., García-Espinosa, J. and Zamora-Parra, B. Non-linear dynamic analysis of the response of moored floating structures. Marine Structures 2016; 49:116-137.

[19] Compassis. SeaFEM Theory Manual. Retrieved from www.compassis.com/soporte. 2016.

[21] Jonkman, J.M. Dynamic modelling and loads analysis of an offshore floating wind turbine, Technical report NREL/TP-500-41958; November 2007.

[22] Fernandes, A. C. and Levy, L. A. P. Cálculo de esforços de onda de primeira e segunda ordem em navios e plataformas flutuantes através de integração azimutal analítica, Congresso da SOBENA (1990). Río de Janeiro, Rj, Brazil.

[23] Kudou, K. The drifting force acting on a three-dimensional body in waves, J.S.N.A. Japan 1977; Vol. 141.

[24] Pinkster, J. A. Low frequency second order wave exciting forces on floating structures. Wageningen: Netherlands Ship Model Basin 650 (1981).

[25] Wojciech, S. Diffraction of second-order surface waves by semisubmerged horizontal rectangular cylinder. J. Waterway, Port, Coastal, Ocean Eng. 1993; Vol 119, 160-171.

[26] Eatock Taylor, R. and Huang, J. B. Semi-analytical formulation for second-order diffraction by a vertical cylinder in bichromatic waves. Journal of Fluids and Structures 1997; 11, 465 – 484.

[27] Shao, Y.L. and Faltinsen, O.M. Numerical Study on the Second-Order Radiation/Diffraction of Floating Bodies with/without Forward Speed. 25th Workshop on Water Waves and Floating Bodies 2010, Harbin, China.

[28] Kim, M.H. and Yue, D.K.P. The complete second-order dif fraction solution for an axisymmetric body. Part 2 : bichromatic incident waves and body motions. J. Fluid Mech. Vol.211, 557-593, 1990.

[29] Moubayed, W.I. and Williams, A.N. Second-Order Hydrodynamic Interactions in An Array of Vertical Cylinders in Bichromatic Waves. Journal of Fluids and Structures, Vol. 9, 61-98, 1995.

[30] http://hiprwind.eu/

[31] https://projects.dnvgl.com/sesam/manuals/Wadam_UM.pdf